Fluorinated Ethylene Carbonate as Additive to Glyme Electrolytes for Robust Sodium Solid Electrolyte Interface

Susmita Sarkar[1+], Matthew J. Lefler[2+], Bairav S. Vishnugopi[1], R. Blake Nuwayhid,[2] Corey T. Love[3], Rachel Carter[3]*, and Partha P. Mukherjee[1]*

[1] School of Mechanical Engineering, Purdue University, West Lafayette, Indiana 47907, USA

[2] NRC/NRL, U. S. Naval Research Laboratory, Washington, DC 20375, USA

[3] Chemistry Division, U. S. Naval Research Laboratory, Washington, DC 20375, USA

[+] denotes equally contributing first authors.

[*] *Correspondence*: rachel.carter@nrl.navy.mil, pmukherjee@purdue.edu

Abstract

The utilization of alkali metal anodes is hindered by an inherent instability in organic electrolytes. Sodium (Na) is of growing interest due to its high natural abundance, but the carbonate electrolytes that are popular in lithium systems are unable to form a stable solid electrolyte interphase (SEI) with a sodium metal electrode. However, the glyme (chain ether) electrolytes produce thin, predominantly inorganic SEI at sodium metal interfaces. Using half-cell and symmetric cell analysis, we identify diglyme (G_2) as the best performing of the glymes, balancing the high nucleation barrier of the short glyme (G_1) and the high plateau overpotential of the long glyme (G_4). Through *in situ* optical microscopy, the onset and growth of Na dendrites are revealed in glyme electrolytes, and the addition of small quantities (~10% volume/volume) of ethylene carbonate (EC) and fluoroethylene carbonate (FEC) to G_2 is shown to facilitate uniform sodium plating characteristics in the optical cell, presumably through alterations to SEI composition. X-ray photoelectron spectroscopy (XPS) analysis reveals that the FEC additive results in an SEI with similar atomic composition to that formed in G_2 alone, whereas the addition of EC to G_2 results in an entirely different SEI composition, despite the molecular similarity of the carbonate additives. We have determined that the SEI formed by glyme alone may not support extensive or extreme cycling conditions, but the addition of FEC provides a much more robust SEI at the Na metal surface to facilitate numerous consistent sodium plating and stripping cycles.

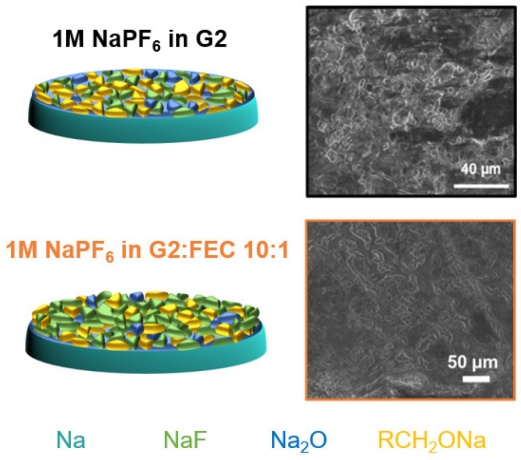

Keywords: sodium metal anode, in-situ optical microscopy, electrolyte additive, solid electrolyte interface

1. Introduction

Alkali metal anodes can enable high-energy-density battery systems due to their low densities and low negative electrochemical potentials.[1-3] Currently, lithium-ion batteries dominate the consumer market for secondary batteries, while newer technologies such as sodium-based systems are gaining tremendous traction driven by the increasing energy storage demands and requirements for battery materials.[4-6] Sodium, much like lithium, is intrinsically a high-energy-density material, but the natural abundance of sodium and other materials used in sodium-based batteries is much higher.[7] This can potentially lower the cost per kWh and help in meeting the wide spectrum of emergent energy storage needs (e.g., grid storage).[2, 8-9]

Despite recent efforts toward understanding sodium metal anodes, further advancement of these metal-based battery systems requires an in-depth analysis of various limitations, including capacity decay, low coulombic efficiencies, and volume changes during cycling.[4, 10] Amongst these, the most critical challenge is the formation of dendrites due to their adverse effect on both the safety and performance of metal-based batteries.[4, 10-13] The suppression of dendrites has been a major focus of the research in alkali metal anodes,[14-22] and a wide range of potential solutions have been examined, including various electrolytes and/or additives,[3, 13, 23-28] utilization of a solid electrolyte,[13, 29-32] and protective films/coatings.[13, 33-38] A unifying theme in most of these studies is related to the modulation of the solid electrolyte interphase (SEI) for enhanced stability of the metal-electrolyte interface. This is the crux of enabling the advancement of sodium battery technologies.[39]

The SEI is typically comprised of insoluble or partially soluble salts that form due to the reductive decomposition of the electrolyte at the metal anode interface.[13, 40-42] This layer acts as a barrier that is both electronically insulating and ionically conductive,[13, 42] and its chemical composition is strongly dependent upon the characteristics of the electrolyte. In conventional carbonate-based electrolytes, organic salts such as HCOO-M, $ROCO_2$-M, or M_2CO_3 are components of the SEI (M=Li, Na). Despite some fundamental similarities, the Li system and Na system are not direct analogs: the lower ionization energy of Na means that it is intrinsically more reactive, and spontaneous interactions of Na with the electrolyte can form an unstable, inhomogeneous SEI that is prone to non-uniformity in electrochemical reactions and morphology evolution.[43] This is one of the factors that differentiate the stability of Na metal electrodes in carbonate electrolytes from Li metal electrodes. However, recent studies demonstrate that sodium

is highly stable in glyme electrolytes, in which thinner, inorganic SEIs are formed.[6, 24, 44-45] In these systems, the SEI is composed mainly of decomposition products from the conductive salts in the electrolyte, with a small contribution from the solvents, e.g., NaF and Na_2O are formed in electrolytes with 1M $NaPF_6$.[13, 23-24, 45-46]

In this study, we examine the addition of cyclic carbonates to glyme electrolytes with the goal of optimizing the plating/stripping of sodium metal. We analyze the plating/stripping behavior and SEI characteristics in sodium metal electrodes with electrochemical impedance analysis, post-mortem scanning electron microscopy (SEM), and physics-based modeling of morphology evolution. Through *in situ* optical microscopy, we reveal the onset of the glyme-based SEI degradation in all three glymes, indicated by dendritic growth, and we explore the stabilizing role of cyclic carbonate (EC and FEC) additives on the plating morphologies. These cyclic carbonates are commonly used in solutions of chain carbonates (EMC, DMC, or DEC) to stabilize the SEI on graphite for Li-ion systems. One previous study of Li metal anodes shows uniform deposition by incorporating cyclic carbonates in a Li-ether system.[47] Based on our modeling framework that captures the wide range of morphologies observed in the experiments; we propose two mechanistic criteria pertaining to the wettability and surface mobility of deposited sodium that critically influence the nucleation behavior and early-stage growth morphologies and are modulated by electrolyte solvent properties. We utilize post-mortem SEM analysis of nanoscale plating morphologies, sodium plating and stripping morphology, and X-ray photoelectron spectroscopy (XPS) characterization of the SEI chemical makeup to comprehensively analyze the superior plating and stripping behavior observed with FEC additive to the glyme electrolyte.

2. Results

First, the underlying difference in sodium nucleation or seed behavior on Cu foil is evaluated in the three different glymes, as shown in **Figure 1a**. Upon fabrication, the cells exhibit open circuit voltages of ~2.4 V. A negative current density of 0.02 mA/cm^2 was applied until 0.04 mAh/cm^2 of sodium was deposited. Before plating is observed ($V > 0$), the SEI is formed. Reduction peaks are observed at ~1.9 V and 0.8 V and account for ~1/4 of the nucleation layer deposition. We confirm that these reduction peaks are a result of irreversible SEI formation by completing 5 cyclic voltammograms from 0 to 2 V (**Figure S1**). The same 1.9 V and 0.8 V peaks are observed only in the first cycle. After the SEI forms in the first cycle, the voltage drops below

0 V, indicating nucleation of sodium metal, and this type of reduction is not observed in subsequent cycles.

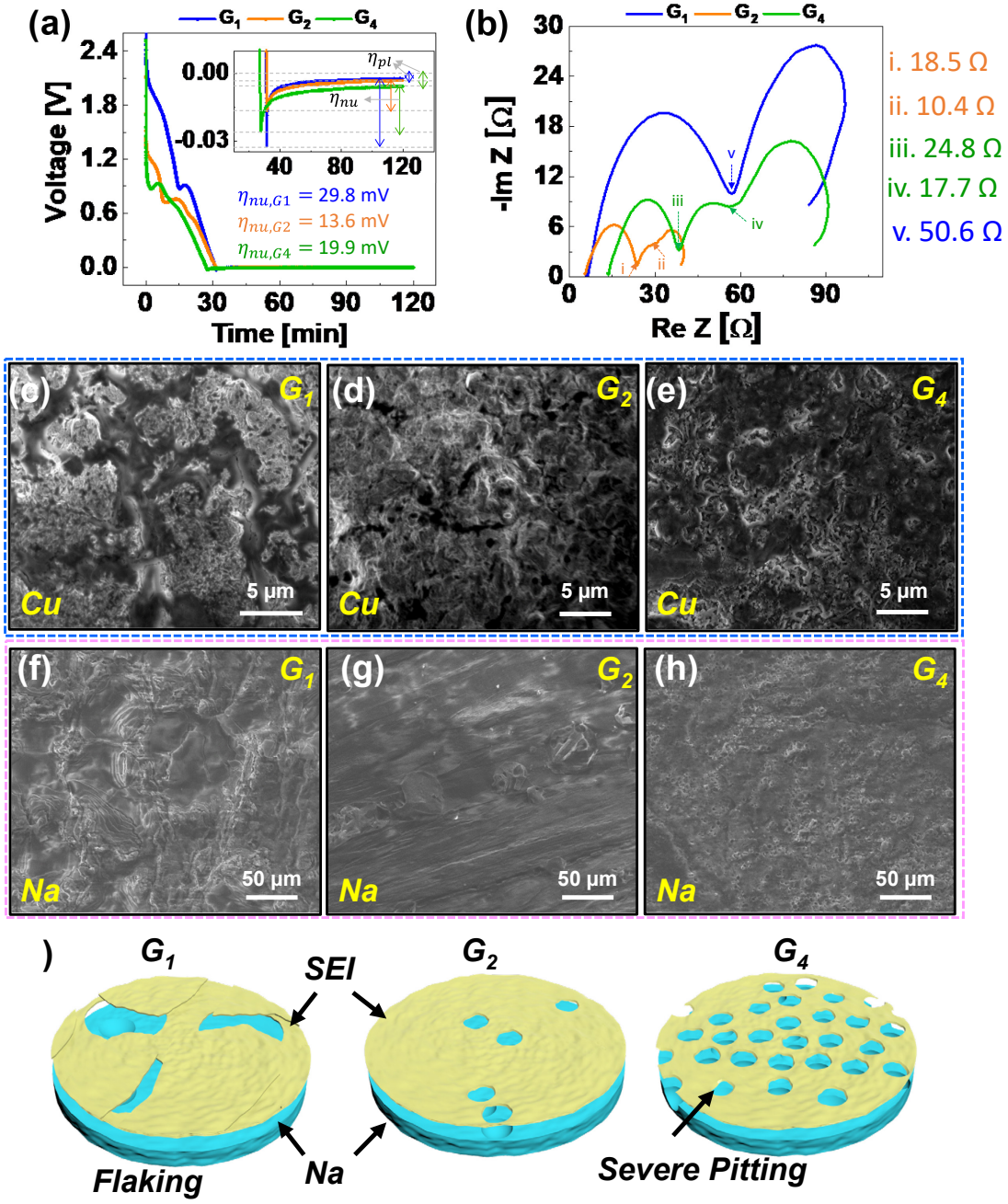

Figure 1. (a) Sodium plating curve for Na|Cu cells in different electrolytes at 0.02 mA/cm^2 and 0.04 mAh/cm^2. (b) EIS of the Na|Cu cells, SEM images of (c)-(e) Cu foil after first deposition and (f)-(g) Na foil after first stripping in different electrolytes. The electrolytes are $NaPF_6$:G_1, $NaPF_6$:G_2, and $NaPF_6$:G_4. (d) Schematic of the stripped Na foil, showing the effect of ether chain lengths on the stripping of Na metal. G_2 shows the least severe stripping.

The sodium deposition process first involves a nucleation overpotential (η_{nu}) during the initial nucleation phase and a mass-transfer overpotential corresponding to further deposition. The post-nucleation signature, also known as plateau potential (η_{pl}), is controlled by mass transfer from the bulk electrolyte through the SEI to the Na nuclei.[48] The nucleation process is energy-intensive and higher than the plateau potential.[49]Monoglyme (G_1) and tetraglyme (G_4) electrolytes exhibit large nucleation barriers (29.8 mV and 19.9 mV, respectively) compared to diglyme (G_2, 13.6 mV), which correlates to the formation of a sporadic and non-uniform Na nucleation morphology. The plateau overpotentials increase with glyme length: G1- 2.4mV, G2- 3.1 mV, and G4- 5.4mV. Of the three glymes, G_2 electrolytes have the smallest η_{nu} and low η_{pl} (3.5 mV), suggesting that a relatively uniform interface with tightly packed Na nuclei is formed while distributing the localized current evenly. In a later section, based on our mesoscale modeling framework, we illustrate how the nucleation characteristics, including the nuclei coverage on the substrate and the early-stage morphology, depend on the competing processes of Na reduction on the substrate and Na reduction on freshly deposited Na. From the electrochemical signatures observed in the experiments, these two processes are correlated to the nucleation (η_{nu}) and plateau overpotential (η_{pl}).

Impedance spectra of Na|Cu cells are analyzed after one cycle to understand the resistivity differences of the cells with G_1, G_2, and G_4 electrolytes. In **Figure 1b**, cells containing G_2 and G_4 electrolytes exhibited two distinct semi-circles in the high- and mid-frequency range, corresponding to SEI resistance and charge-transfer resistance, respectively. A much smaller impedance is obtained for G_2 cells (R_{SEI}+R_{CT} ≈ 29 Ω), as opposed to that of G_1 cells (R_{SEI}+R_{CT} ≈51 Ω) and G_4 cells (R_{SEI}+R_{CT} ≈42 Ω). Additionally, the Cu electrode in G_4 cells shows a relatively higher solution resistance compared to the other glymes, likely due to its higher viscosity (**Table 1**). These impedance results are in line with the lower nucleation overpotentials for G_2 relative to G_1 and G_4, as well as better cycling stability arising from uniform deposition observed in cells with G_2 electrolyte, which is later discussed in **Figure 2**. **Table S1** summarizes the nucleation barrier, plateau overpotential, and impedances for the different glyme electrolytes and **Figure S2** shows the as fabricated EIS.

Table 1- solvent names and material properties for electrolytes investigated

Abbreviation	*name*	*Compound*	*Dielectric Constant (25°C)*	*Viscosity (mPa*s; 25°C)*	*Donor No*
G_1	monoglyme	$CH_3OCH_2CH_2OCH_3$ 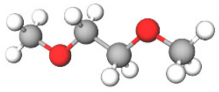	7.2	0.42	24
G_2	diglyme	$(CH_3OCH_2CH_2)_2O$ 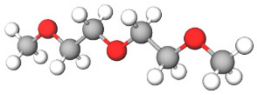	7.3	0.98	19.5
G_4	tetraglyme	$CH_3O(CH_2CH_2O)_4CH_3$ 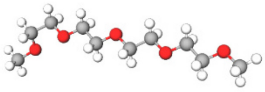	7.9	3.7	16.7
EC	ethylene carbonate	$C_3H_4O_3$ 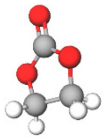	89.78	1.93 (40°C)	16.4
FEC	fluoroethylene carbonate	$C_3H_3FO_3$ 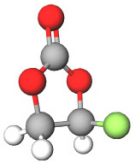	79.7	4.1	7.9

Na plating and dissolution processes for Na|Cu is further analyzed by SEM characterization in **Figure 1c-h**. During the plating process, the bright regions imaged exhibited uniform sodium deposition facilitating electron microscopy through the conductive surface. However, darker regions with surface fractures indicate the formation of insulating species via undesirable side reactions, especially in the G_1 electrolyte, **Figure 1f-h**. During the stripping process, Na metal in the presence of G_1 electrolyte is observed to result in flaky, pulverized surface structures (**Figure 1f**), indicating the non-uniform distribution of reaction current. In the G_2 electrolyte, Na stripping resulted in the formation of small pinhole-like structures, as seen in **Figure 1g**. However, in the G_4 electrolyte, a higher density of void and pit formation is observed, shown in **Figure 1h**. The aggregation of these voids can lead to the evolution of big craters, causing rupture and detachment

of the SEI [50-52]. In addition to the SEI morphologies shown in **Figure 1c-h, Figure 1i** represents our conceptual understanding of these SEI behaviors in each electrolyte condition.

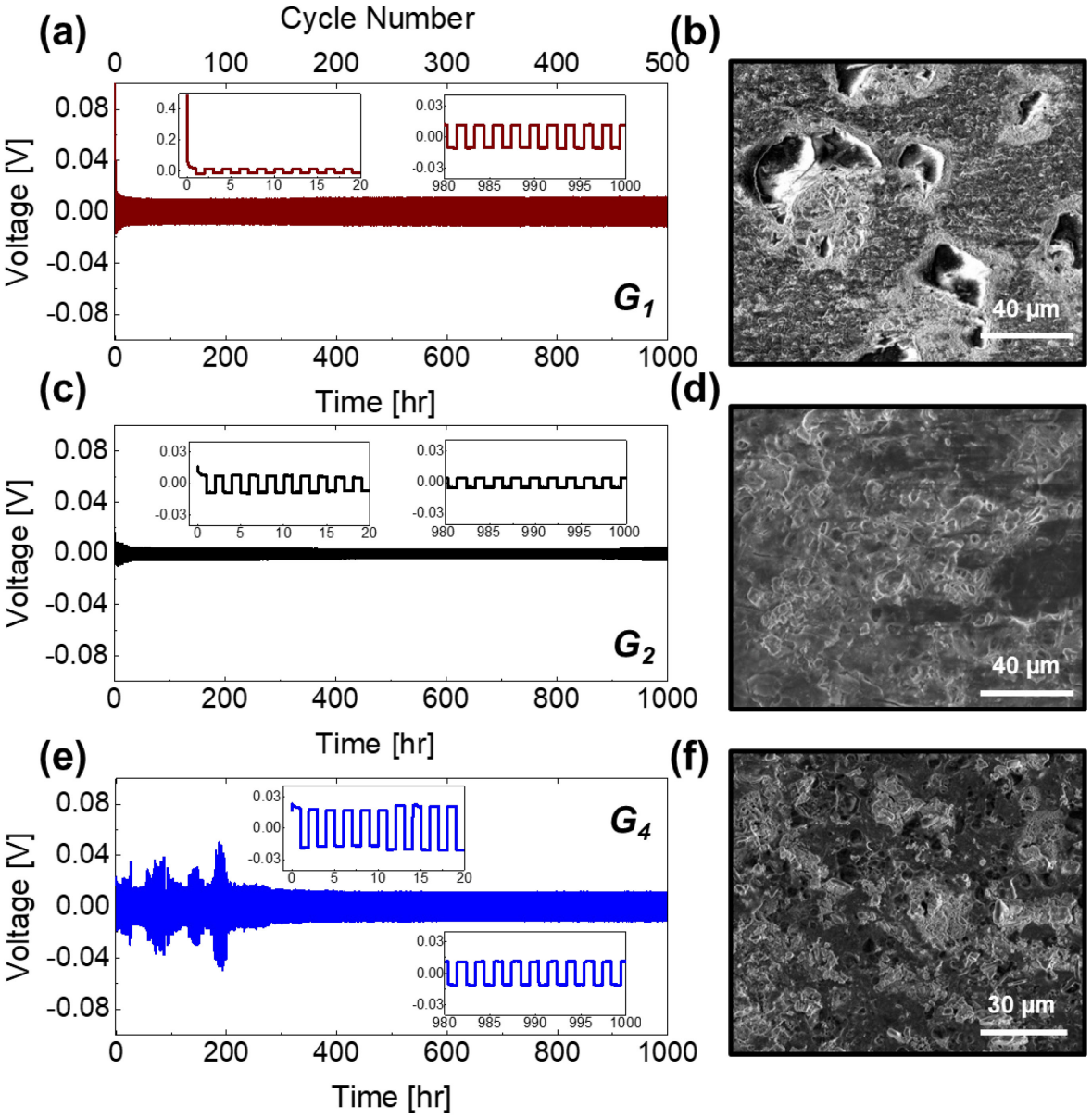

Figure 2. Plating-stripping profiles of Na|Na cells at a current density of 0.5 mA/cm^2 and capacity of 0.5 mAh/cm^2 in (a) G_1, (c) G_2, and (e) G_4. SEM Images of the Na foil after 10 charge-discharge cycles in (b) G_1, (d) G_2, and (f) G_4. G_4 shows erratic voltage hysteresis, and the SEM image shows mossy, needle-like Na deposits localized in the pit-like holes.

With evidence that G_2 provides the most desirable seed layer among the glymes, long-term cycling stability was explored in Na|Na cells using 1M $NaPF_6$ in G_1, G_2, and G_4. **Figure 2** shows the cycling performance at a constant current density of 0.5 mA/cm^2 and Na deposition capacity of 0.5 mAh/cm^2. The inset figures show the first 20 hours of plating and stripping and the last 20 hours of plating and stripping. In G_1 (**Figure 2a**), the initial plating process presents a distinctly large overpotential drop of ~0.5 V, likely due to the high nucleation barrier required for the Na plating process to begin, as seen in the seed layer investigation in **Figure 1**. Subsequent plating and stripping cycles experience a voltage hysteresis of 12.9 ± 2 mV in G_1, where voltage hysteresis is defined as the average of the difference in voltage between plating and stripping of each cycle ($V_{max,\ stripping} - V_{min,\ plating}$)/2.[53] In G_2 (**Figure 2c**), we observe not only minimal overpotential to the first plating process, but also the smallest voltage hysteresis to symmetric cycles (6.5 ± 2 mV). Finally, in G_4 (**Figure 2e**), though there is a small overpotential corresponding to the first plating process, the highest voltage hysteresis is observed (~20 mV).

Figures 2b, **d**, and **f** are SEM images of electrodes from cells disassembled after 10 plating/stripping cycles in G_1, G_2, and G_4, respectively. In G_1 (**Figure 2b**), large (~30 μm), rounded shapes are observed on the metal surface.[48] In the cells with the G_2 electrolyte (**Figure 2d**), the Na metal appears to have a uniform surface coverage, but the G_4 electrolyte (**Figure 2f**) shows signs of dendritic growth all across the electrode surface. The SEM shows severe mossy and needle-like Na deposits localized in the pit-like holes, indicating the instability of the metal anodes in this electrolyte.

To examine the long-term stability of each glyme system, the symmetric cells operated for a total of 2500 hours, or 1250 cycles (full data set in **Figure S3**). In the G_1 cell, the voltage hysteresis gradually grew with cycling to approach 20 mV, and the G_2 cell, which initially displayed the smallest voltage hysteresis and likely the thinnest SEI, exhibits a stark increase to ~30 mV after about 768 cycles or 1536 hours of operation, indicating long-term risk to this system. Finally, the behavior of the G_4 system is initially erratic, indicating potential soft shorts, followed by a gradual increase in hysteresis to ~30 mV.

Figure 2 identifies G_2 as the glyme with a minimal initial plating overpotential, the lowest voltage hysteresis to plating and stripping (6.5 ± 2 mV), and the smoothest surface morphology in SEM analysis. However, extensive cycling leads to increased voltage hysteresis and more unstable behavior. We hypothesize that despite the favorable initial morphology in this electrolyte,

extensive or abusive cycling will result in the breakdown of the SEI and undesirable plating/stripping behavior. In order to exacerbate these effects, we utilize *in-situ* optical microscopy to observe the onset of dendrite formation in real time. This setup is described and depicted in our previous work.[54] The construction of the optical cell utilizes a spatial separation technique instead of a physical separator material; consequently, this cell configuration lacks stack pressure, which is a well-known technique for suppressing dendritic behavior, and thus, dendritic growth is allowed to proceed without hindrance in the optical cell configuration.[55] In addition, we also probe the effect of carbonate additives to diminish the propensity for dendritic onset and facilitate extensive cycling by providing chemical complexity and mechanical rigidity to the SEI.

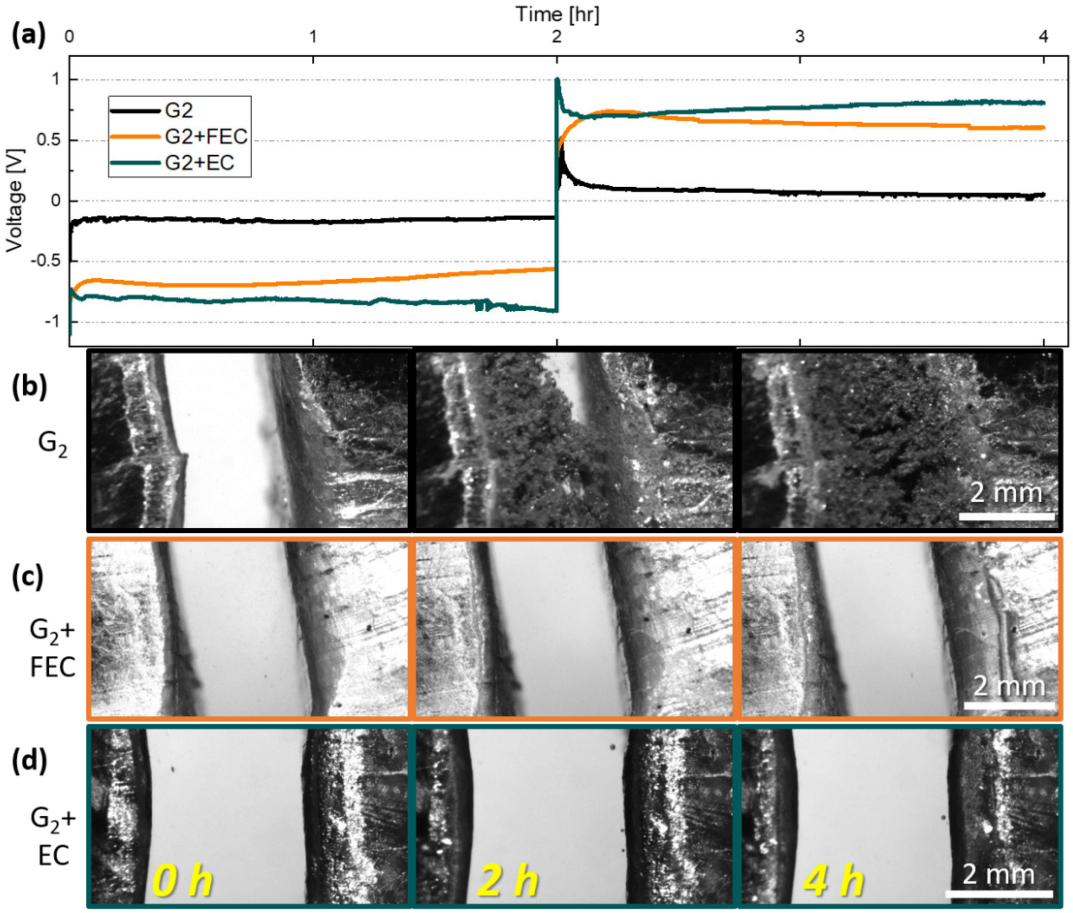

Figure 3. Voltage profiles and optical cell images of symmetric Na cells in electrolytes of 1M $NaPF_6$ in G_2, G_2+FEC 10% v: v, and G_2+EC 10% v:v. Images of the optical cell are shown at t = 0 h (left), 2 h (middle), and 4 h (right). Pure G_2 electrolyte, without any additive, non-uniform Na dendrites can be observed. With FEC and EC added to the electrolyte, dendrite formation is eliminated, which is mostly achieved by tuning the SEI with favorable properties

Sodium stripping and plating in pure G_2 electrolyte at a current density of 0.75 mA/cm^2 lead to significant morphological changes in the sodium electrodes, **Figure 3a**. While the sodium was stripped from one electrode, pitting occurred on the surface of that electrode, causing severe roughing of the electrode surface. On the other electrode, uneven plating and dendrites were observed to form almost immediately. These dendrites quickly fill the gap between the two electrodes, initiating a short circuit between the two electrodes. Video of this cell can be found in the SI, **Video S2.**

In stark contrast, the addition of 10 vol% FEC (approx. 1.4M) to the G_2 electrolyte appears to mitigate the formation of dendritic structures, shown in **Figure 3c** and **Video S4**. The stripping and plating processes occur without the pitting and problematic growths seen in the pure glyme electrolyte, though the surface of the sodium electrode does change slightly in appearance during the application of a current. This layer, while challenging to detect in the images in **Figure 3c**, can be observed in the videos of the optical cells shown in the SI. We hypothesize that the surface layer that appears during plating and fades during stripping might be the protective SEI, which decomposes with the switch in polarization since the improved morphology is coupled with an increased voltage hysteresis, likely due to a more complex SEI.

As FEC is a derivative of EC (see **Table 1**), this more common carbonate was also studied in these systems for comparison. With an equivalent amount of EC additive in the G_2 electrolyte, the behavior is comparable to FEC in terms of sodium electrode stability during the experiment, although the voltage profile in **Figure 3a** shows that there is a higher overpotential when EC is used in place of FEC. G_1 electrolyte was also studied in the optical cell, and the results, shown in the SI, are similar to those of G_2, such that the FEC and EC additives provide an environment for a more stable Na electrode.

When employing an EC or FEC additive in the G_1 electrolyte at approximately 1.4M, multiple cycles of the Na|Na cell can be achieved without significant change to the sodium electrodes, as demonstrated in **Figure S12**. Experiments in which the molarity of the EC additive was decreased provided insight into this method of electrode protection. When the concentration of the EC additive was halved, there was a slight delay before dendrite formation initiated; however, the morphology of the dendrites in glyme electrolytes with lower carbonate levels was very different from those formed in the pure glyme electrolyte. Whereas without carbonate additive, the dendrites quickly formed mossy structures (as described by Frenck et al. [56]), with the addition of

carbonate, the metallic growths formed much finer dendrites that reached across the gap to create a short circuit, indicating that the carbonate additive changes not only the chemistry of the SEI, but also the mechanical properties. Continuation of the experiment led to more of these dendrites forming a mesh-like construct between the two electrodes, eventually creating a solid structure that bridged the gap between the electrodes (**Video S7**). One possible explanation for this change in dendritic morphology has been reported in a recent study by Boyle et al., in which the authors state that the solvation tendencies of the electrolyte play a large part in the morphology of the resulting plated metal. FEC, described as a weakly solvating electrolyte, thermodynamically favors a more uniform alkali metal plating due to increased surface energy, whereas EC, a strongly solvating electrolyte, lowers the surface energy at the electrode, thus favoring a high surface area growth pattern (dendrites).[57] This could be the reason for the finer (higher surface area) structure of the dendrites observed in the EC-containing system. Observation of this progression of sodium electrodeposition indicates that the presence of carbonate inhibits dendritic growth and that small amounts of carbonate initially protect the sodium electrode but are easily overwhelmed. This also implies a correlation between the concentration of carbonate additive and the strength and stabilizing role of the SEI formed on the electrode.

Based on these promising findings, additional investigation of the glyme system with carbonate additives was completed in closed coin cell systems. Na|Na symmetric cell performances of FEC-containing electrolytes with 2 separators are shown in **Figure 4**. It should be noted that irregular voltage behavior was observed while using one separator (**Figure S6)**, which is likely evidence of soft shorts. This was remedied by adding an extra separator, resulting in steady voltage hysteresis. Compared to a pure glyme electrolyte, this glyme+FEC system produced a larger overpotential, likely due in part to the higher viscosity associated with the addition of FEC (**Table 1**) [58-59] and supported by the calculated η_{nu} values for G_2 (≈13.6 mV), and G_2+FEC (≈62.4 mV). Inset of initial cycle profiles is shown in **Figure 4a** and the final cycles in Figure S7. SEM images in **Figure 4b** indicate that Na stripping/plating in G_2+FEC results in a more smooth morphology of the electrode surface compared to pure G_2 electrolyte (**Figure 2b**). This finding is supported in **Figures 3b and c**, in which the results of stripping and plating reactions in both G_2 and G_2+FEC electrolytes are shown the optical cell, and it is clear that the addition of FEC has resulted in a vastly improved Na plating morphology.

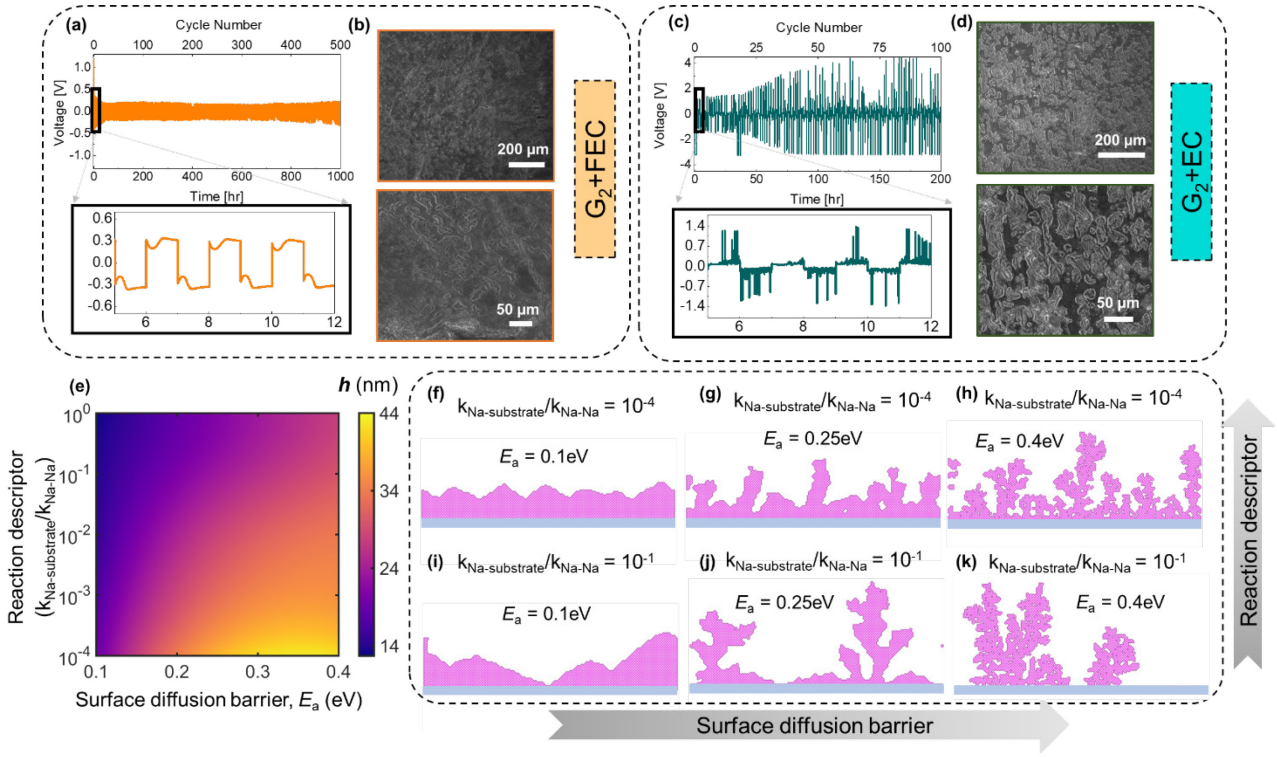

Figure 4. Plating-stripping profile of Na-Na cells in different electrolytes at 0.5 mA/cm^2 and 0.5 mAh/cm^2 (a) G_2+FEC and (c) G_2+EC. SEM images of the Na foil after 10 charge-discharge cycles show distinct morphologies in each of the electrolytes. (e) Electrodeposit height (h) and (f-k) corresponding morphological pattern depicted as a function of the reaction descriptor ($k_{Na\text{-}substrate}/k_{Na\text{-}Na}$) and surface mobility of the deposited metal atoms.

The same systems were studied in electrolyte with EC additive. Despite the seemingly stable performance in the optical cell and similar properties of the two additives (**Table 1**), the Na electrode in G_2+EC succumbs to dramatic voltage fluctuations from the beginning of cycling. Voltage spikes up to 4 V are observed; a phenomenon often correlated to dendritic growth.[13] SEM images (**Figure 4d**) reveal the typical morphology of plated/stripped Na metal after 10 cycles in G_2+EC. Compared to the electrolyte with FEC additive, the Na growth in these samples was very non-uniform and dendritic. SEM images of the surface morphology reveal a porous and inconsistent SEI, which prevents proper protection of sodium metal against the corrosive organic electrolyte. It is hypothesized that the mechanical properties of the G_2+EC derived SEI are less ideal than the G_2+FEC since both seem to prevent dendritic growth in the *in situ* optical cells free from compression, but in symmetric coin cells, the G_2+EC electrolyte results in erratic behavior.

To mechanistically understand the nucleation/growth behavior, we develop a mesoscale model that captures the dynamic evolution of the metal electrode morphology. The modeling framework is based on the kinetic Monte Carlo approach and examines the role of competing processes, including electrochemical reaction on the substrate, growth of the nucleated deposit, migration of the deposited atoms, and ion transport.[60-62] A detailed description of the modeling framework and parameters are presented in the Supporting Information. As observed in the experiments (**Figure 1a**), a key aspect that governs the nucleation behavior is the difference in preference for deposition to occur on the pristine substrate versus the freshly nucleated Na deposits. Depending upon the electrolyte, this difference is discerned in the experiments based on the distinct nucleation and plateau overpotential signatures (**Figure 1a**). In our modeling framework, we introduce a descriptor, $k_{\text{Na-substrate}}/k_{\text{Na-Na}}$, to study this competing process that occurs during nucleation. Here, $k_{\text{Na-substrate}}$ refers to the reaction rate for Na reduction on the pristine substrate, and $k_{\text{Na-Na}}$ refers to the reaction rate for Na reduction on the freshly formed Na deposits on the substrate. We note that the simulations have been carried out until a total of 2000 Na atoms have been deposited. As shown in **Figure 4e**, with an increase in $k_{\text{Na-substrate}}/k_{\text{Na-Na}}$, a decrease in dendritic height (h) is illustrated. Physically, this denotes a regime of smooth plating driven by the enhanced metal-substrate interaction. This mechanism is responsible for the reduced dendritic height that is observed in **Figure 4e** as a function of $k_{\text{Na-substrate}}/k_{\text{Na-Na}}$. By modulating this descriptor ($k_{\text{Na-substrate}}/k_{\text{Na-Na}}$) as well as surface mobility, we can investigate the influence of these properties on deposition morphologies, as shown in **Figure 4f** - **Figure 4k**. We observe an increase in the number of nuclei and utilization of the substrate with an enhancement in $k_{\text{Na-substrate}}/k_{\text{Na-Na}}$, and the growth patterns transition from dendritic, to mossy to smooth as the surface mobility increases.

We hypothesize that this is the underlying descriptor for the difference in nucleation density and early-stage growth morphologies observed across the different glyme electrolytes. From the morphologies captured by the model, we understand that $k_{\text{Na-substrate}}/k_{\text{Na-Na}}$ affects the substrate coverage and nucleation density that characterize the initial uniformity, which is potentially correlated to transport properties of the electrolytes like solvent viscosity and their substrate wettability. The surface mobility dictates deposition morphology and is impacted by the solvent-derived SEI.[63] G_2 has the lowest viscosity of the solvents (**Table 1**), leading to a high degree of wettability and a large nucleation density.[24] The experimentally observed morphology with the G_2 electrolyte correlates with the morphological pattern in **Figure 4h**, denoting a

mechanistic regime with low surface mobility. The addition of high viscosity carbonates, EC and FEC,[16] shifts the morphology down a row (i.e., reduced wettability), such that the observed morphologies of G_2+EC and G_2+FEC align with **Figure 4j** and **Figure 4i**, respectively. This correlation suggests that the SEI from the G_2 + FEC electrolyte improves surface mobility when compared to the G_2 + EC electrolyte, thereby resulting in a smoother electrodeposition growth response. The modeling results emphasize the critical role of SEI chemistry (e.g., due to additives like FEC/EC) in the manifestation of distinct morphological growth regimes despite similar nucleation trends. In turn, the morphological evolution of the metal and the resulting volume expansion affect the mechanical stability of the SEI.

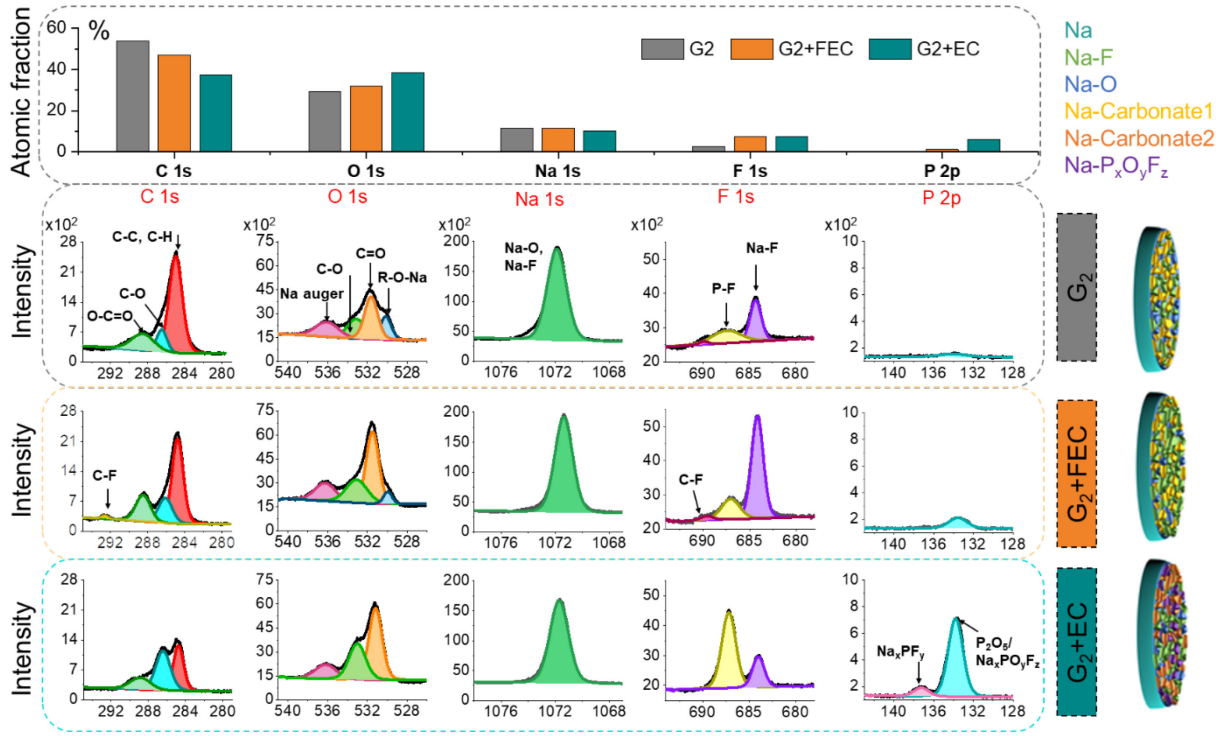

Figure 5. XPS characterization of Na foil anode SEI after 10 charge-discharge cycles in Na|Na cell setup. The atomic percentage of different elements is compared in the top row. The C 1s, O 1s, Na 1s, F 1s, and P 2p spectra for G_2, G_2+FEC, and G_2+EC electrolytes are shown. Schematic representation of mosaic SEI formed in each electrolyte is provided on the right.

Although EC and FEC are analogs, when added to glymes, the sodium plating and stripping behaviors in each solution are distinct. Mesoscale modeling and optical investigation suggest that the mechanical properties of their derived SEIs can be dissimilar. Therefore, air-sensitive XPS

analysis was used to investigate the chemical makeup of the SEI formed in G_2, G_2+FEC, and G_2+EC electrolytes. After 10 cycles, coin cells were deconstructed in a glovebox, and the sodium surface was washed with the glyme solvent to remove the salt species. SEM of replicate cells is found in **Figure S9**. When first comparing the atomic percentages present at the electrode surface, the atomic ratio of carbon (from C 1s) decreases from G_2 to G_2+FEC to G_2+EC, while oxygen (O 1s) increases. This correlates to a transition from glyme-derived hydrocarbon components to complex carbonates in the SEI. Next, a slight decrease in sodium concentration (Na 1s) is observed in G_2+EC, which may affect sodium ion conductivity. Most notably, compared to G_2, both G_2+FEC and G_2+EC see an increase in fluorine (F 1s). Fluorinated species, such as NaF, are known to be desirable components of the SEI, as they provide high ionic conductivity and beneficial mechanical properties.[24, 64] Finally, phosphorous is only detected in appreciable quantities in the G_2+EC sample, suggesting that the fluorine found in this sample is bound to phosphorus as P-F species derived from the $NaPF_6$ salt.

Looking closer at the C 1s spectrum of the electrode in G_2 electrolyte, three characteristic peaks are observed around 285 eV, 286 eV, and 289 eV, which correlate to species derived from the decomposition of G_2, particularly alkoxides, esters, and ethers.[24, 65] However, the proportion of the C–C/C–H equalizes with the C-O bond in the G_2+EC electrolyte, indicating additional species derived from the EC.[66] EC is known to reduce into the reactive and complex sodium ethylene dicarbonate, or NEDC ($NaO_2CO–C_2H_4–OCO_2Na$).[6, 67] This more complex SEI explains high charge transfer resistances, making it difficult for the ions to move through the energy barrier. We see evidence of this with increased voltage hysteresis in **Figures 3** and **4**.

The O 1s spectrum for all three electrolytes shows a significant peak at ~531.2-531.6 eV ascribed to C=O, presumably related to carbonates present in the SEI. The peak at ~533.1 eV indicates the presence of C-O and is much more prominent in the G_2+EC electrolyte, which may also be due in part to the formation of NEDC.[65, 68] Additionally, metal oxides typically have binding energies near ~530 eV, which appears in these spectra as Na-O, which might take the form of a sodium alkoxide or other complex SEI components.

Fluorine is observed in all samples as a result of the decomposition of the fluorine-containing $NaPF_6$ salt. The F 1s spectrum shows two distinct peaks at ~687 eV and ~684 eV, corresponding to P-F and Na-F bonds, respectively, where P-F indicates incomplete decomposition of $NaPF_6$, and Na-F indicates the formation of NaF, a desirable SEI component, at the surface. An

additional weak C-F peak can be seen in the spectra of G_2 and G_2+FEC, which derives from the reduction of the G_2 solvent in conjunction with the decomposition of the salt, though contributions from this are minimal. Further, in G_2+FEC electrolyte, the reduction of the FEC solvent leads to the formation of a significant amount of desirable Na-F bonds. However, with the addition of EC, the intensity of Na-F becomes very weak, and the P-F portion becomes stronger. This reveals that the different cyclic carbonates facilitate distinct SEI formations, such that FEC enables the production of more Na-F, while EC traps P-F salt anions and suppresses Na-F formation.

Since $NaPF_6$ is the salt used in each electrolyte condition, phosphate compounds are expected to be present in the SEI. However, the G_2 and G_2+FEC electrolytes show almost no peaks in the P 2p region. In contrast, the G_2+EC electrolyte shows a large phosphate peak, attributed to P_2O_5 and $Na_xPO_yF_z$, and a smaller P-F peak, attributed to Na_xPF_y. This further supports the idea that EC causes the decomposition of the electrolyte salt at the SEI, unlike the pure G_2 and G_2+FEC cases.

When comparing the metal anode in different electrolytes, the prominent differences are the relative amount of C-O, C=O, and Na-F. The inorganic species, NaF, derived from PF_6^- salt or FEC, plays a crucial role in stabilizing the overall SEI. Na-F levels are highest in G_2+FEC and lowest in G_2+EC, and C-O is highest in G_2+EC and lowest in G_2 alone. Schematic representation of the resulting SEI depicts the G_2 SEI to be thin and composed of primarily NaF, Na_2O, and G_2-derived carbonates, denoted "Carbonate1." G_2+FEC exhibits a thicker SEI with the same components as G_2 alone but with a higher concentration of the desirable NaF component. And G_2+EC contains a thicker SEI but with entirely different complex carbonate components, denoted "Carbonate2," and salt derivatives ($Na_wP_xO_yF_z$).

3. Conclusion

In situ optical microscopy, half cells, and symmetric cells were used to identify robust sodium plating and stripping in ether electrolytes with and without carbonate additives. The stability of sodium electrodes in glyme ether family electrolytes was investigated with extensive cycling and an *in situ* optical cell. The shortest length glyme, G_1, presents a high nucleation barrier and lower growth barrier in the first plating voltage profile, suggesting the formation of Na clusters as the Na adatom can easily form on existing nuclei. Alternatively, G_4 possesses a high voltage hysteresis as a result of higher viscosity and shows evidence of severe pitting in SEM investigation.

G_2 provides a desirable middle condition in the glyme family, mitigating the high nucleation overpotential of G_1 and the high hysteresis of G_4. However, the hysteresis in G_2 builds over many cycles in the symmetric system. Further, in the investigation of G_2 electrolyte in an optical cell, unstable dendritic growth was observed without the presence of pressure or a separator material. We then observed the addition of cyclic carbonate to provide mechanical rigidity to the SEI and facilitate a longer cycle life. FEC and EC were investigated with *in situ* optical microscopy, and though both additives showed smoothed sodium plating morphologies, higher voltage hysteresis was observed due to SEI thickening. Symmetric cell assessment of the FEC additive provided stable plating and stripping over many cycles; however, the EC additive resulted in erratic potential in symmetric coin cells. SEM analysis reveals poor SEI morphology with the EC additive but much-improved surface morphology with the addition of FEC compared to G_2 alone. These findings indicate that the FEC additive leads to a thicker, more robust SEI, promising longer cycle life or more extreme cycling conditions.

Since FEC and EC are very similar in structure and properties, we utilized XPS analysis to confirm that the two solvents produce molecularly different SEIs. Mesoscale modeling hints that SEI composition and rigidity strongly influence plating morphologies. Compared to G_2, the addition of EC to the electrolyte results in an entirely different atomic composition at the electrode surface after 10 cycles. This SEI was dominated by complex carbonate compounds and phosphorous- and fluoride-containing compounds derived from salt decomposition, while the FEC additive maintained low concentrations of G_2-derived carbonates and high NaF concentration, mirroring the desirable SEI components of the thin G_2 SEI. Among the electrolytes investigated, our work identifies 1M $NaPF_6$ in G_2:FEC in a 90/10% v:v as optimal for sodium plating and stripping. This electrolyte facilitates a NaF-rich SEI that is robust and prevents dendritic growth. Further experimentation is necessary to determine the optimal carbonate concentration in glyme electrolytes to maximize the performance gain with FEC concentration.

4. Experimental Methods

Materials:

Diethylene glycol dimethyl ether (diglyme, Sigma-Aldrich, anhydrous, 99.5%)

1,2-Dimethoxyethane (DME, monoglyme, Sigma-Aldrich, anhydrous, 99.5%)

$NaPF_6$ (STREM chemical, 99.99% Na, PURATREM)
Fluoroethylene carbonate (FEC, Sigma-Aldrich, 99%)
Ethylene carbonate (EC, Sigma-Aldrich, anhydrous, 99%)
Cu foil from (MTI 9 μm)
Entek Gold 20 μm
Sodium Metal (650 μm Sigma Aldrich)

Coin cell:

The electrochemical performances were measured in a CR-2032 coin cell format either using a Na|Cu or Na|Na setup using different electrolyte solvents using a NEWARE Battery Tester. The electrolytes are pure ether solvents (1.0 M $NaPF_6$ in G_1, G_2 and G_4) and the ether-carbonate electrolyte mixtures (1.0 M $NaPF_6$ in G_1+EC, G_1+FEC, G_2+EC, G_2+FEC, G_4+FEC). 90 μL of electrolyte were added to all cells. 1 separator was used with all pure glyme electrolytes: G1, G2, and G4. When FEC or EC were added, 2 separators were used. The areal loading of sodium was 370 mg/cm^{2,} and the sodium was oversized by 8X. Biologic was used to do the Potentio EIS (PEIS) in a frequency range of 1 MHz to 0.1 Hz at 20 ± 2°C. Long-term cycling was confirmed with 2 cells. More than 10 cells were tested up to 10 cycles and examined with post-mortem analyses.

Optical cell:

The experiments described here are visualized with the optical cell. The optical cell is fabricated by sandwiching an inner Teflon plate, machined with a rectangular central gap approximately 3.00 mm wide by 6.25 mm in length, with two acrylic outer plates containing quartz windows. To make symmetric cells, electrodes of copper foil with sodium deposited on them are threaded through the inner hole of the Teflon plate and pulled taut opposite each other, and the cell is constructed with Viton gaskets between the plates to contain the electrolyte that is injected into the cell. The cell is described in more detail in Love et al. and Carter et al.[54, 69] The electrolyte is composed of a glyme as the main component (either monoglyme, G_1, or diglyme, G_2) and 1M $NaPF_6$ as the conductive salt. Ethylene carbonate and fluoroethylene carbonate are used as additives at 10% by volume for FEC and equivalent molarity (~1.4M) for EC. Sodium symmetric cell experiments were performed at 0.2 mA, or approximately 0.75 mA/cm^2, with a polarity switch occurring every 2 h.

Surface Characterization:

The surface morphologies were observed using a scanning electron microscope (SEM) (FEI Nova nanoSEM).

Conflicts of interest

There are no conflicts to declare.

Acknowledgments

This work was supported by NRL based Program through the Office of Naval Research. P.P.M. acknowledges support in part from the Office of Naval Research (ONR award: N00014-19-1-2529) and National Science Foundation (NSF award: 1805656). This research was performed while Matthew J. Lefler held an NRC Research Associateship award at the U.S. Naval Research Laboratory.

Supporting Information

EIS of Fresh Na-Cu cells, the plating-stripping profile of Na-Na cells in different glyme electrolytes, discharge curve, EIS of Na-Cu, symmetric cell performance, SEM images, video microscopy images of the Na metal in different glyme electrolytes with FEC and EC additive, and description of the mesoscale modeling framework and parameters.

References

1. Lin, D.; Liu, Y.; Cui, Y. (2017). Reviving the lithium metal anode for high-energy batteries. Nature Nanotechnology *12*, 194-206.
2. Park, R. J. Y.; Eschler, C. M.; Fincher, C. D.; Badel, A. F.; Guan, P.; Pharr, M.; Sheldon, B. W.; Carter, W. C.; Viswanathan, V.; Chiang, Y.-M. (2021). Semi-solid alkali metal electrodes enabling high critical current densities in solid electrolyte batteries. Nature Energy *6*, 314-322.
3. Zheng, J.; Chen, S.; Zhao, W.; Song, J.; Engelhard, M. H.; Zhang, J.-G. (2018). Extremely Stable Sodium Metal Batteries Enabled by Localized High-Concentration Electrolytes. ACS Energy Letters *3*, 315-321.
4. Liu, H.; Osenberg, M.; Ni, L.; Hilger, A.; Chen, L.; Zhou, D.; Dong, K.; Arlt, T.; Yao, X.; Wang, X.; Manke, I.; Sun, F. (2021). Sodiophilic and conductive carbon cloth guides sodium dendrite-free Na metal electrodeposition. Journal of Energy Chemistry *61*, 61-70.

5. Fan, L.; Li, X. (2018). Recent advances in effective protection of sodium metal anode. Nano Energy *53*, 630-642.
6. Ferdousi, S. A.; O'Dell, L. A.; Hilder, M.; Barlow, A. J.; Armand, M.; Forsyth, M.; Howlett, P. C. (2021). SEI Formation on Sodium Metal Electrodes in Superconcentrated Ionic Liquid Electrolytes and the Effect of Additive Water. ACS Applied Materials & Interfaces *13*, 5706-5720.
7. Larcher, D.; Tarascon, J. M. (2015). Towards greener and more sustainable batteries for electrical energy storage. Nature Chemistry *7*, 19-29.
8. Hu, Y.-S.; Lu, Y. (2019). 2019 Nobel Prize for the Li-Ion Batteries and New Opportunities and Challenges in Na-Ion Batteries. ACS Energy Letters *4*, 2689-2690.
9. Palomares, V.; Serras, P.; Villaluenga, I.; Hueso, K. B.; Carretero-González, J.; Rojo, T. (2012). Na-ion batteries, recent advances and present challenges to become low cost energy storage systems. Energy & Environmental Science *5*, 5884.
10. Zhu, M.; Li, S.; Li, B.; Gong, Y.; Du, Z.; Yang, S. (2019). Homogeneous guiding deposition of sodium through main group II metals toward dendrite-free sodium anodes. Science Advances *5*, eaau6264.
11. Ye, L.; Liao, M.; Zhao, T.; Sun, H.; Zhao, Y.; Sun, X.; Wang, B.; Peng, H. (2019). A Sodiophilic Interphase-Mediated, Dendrite-Free Anode with Ultrahigh Specific Capacity for Sodium-Metal Batteries. Angewandte Chemie International Edition *58*, 17054-17060.
12. Chen, X.; Bai, Y.-K.; Shen, X.; Peng, H.-J.; Zhang, Q. (2020). Sodiophilicity/potassiophilicity chemistry in sodium/potassium metal anodes. Journal of Energy Chemistry *51*, 1-6.
13. Lee, B.; Paek, E.; Mitlin, D.; Lee, S. W. (2019). Sodium Metal Anodes: Emerging Solutions to Dendrite Growth. Chemical Reviews *119*, 5416-5460.
14. Zheng, J.; Kim, M. S.; Tu, Z.; Choudhury, S.; Tang, T.; Archer, L. A. (2020). Regulating electrodeposition morphology of lithium: towards commercially relevant secondary Li metal batteries. Chemical Society Reviews *49*, 2701-2750.
15. Xiang, J.; Yang, L.; Yuan, L.; Yuan, K.; Zhang, Y.; Huang, Y.; Lin, J.; Pan, F.; Huang, Y. (2019). Alkali-metal anodes: from lab to market. Joule *3*, 2334-2363.
16. Wang, H.; Yu, D.; Kuang, C.; Cheng, L.; Li, W.; Feng, X.; Zhang, Z.; Zhang, X.; Zhang, Y. (2019). Alkali metal anodes for rechargeable batteries. Chem *5*, 313-338.
17. Liu, H.; Cheng, X.-B.; Jin, Z.; Zhang, R.; Wang, G.; Chen, L.-Q.; Liu, Q.-B.; Huang, J.-Q.; Zhang, Q. (2019). Recent advances in understanding dendrite growth on alkali metal anodes. EnergyChem *1*, 100003.
18. Vishnugopi, B. S.; Kazyak, E.; Lewis, J. A.; Nanda, J.; McDowell, M. T.; Dasgupta, N. P.; Mukherjee, P. P. (2021). Challenges and opportunities for fast charging of solid-state lithium metal batteries. ACS Energy Letters *6*, 3734-3749.
19. Aslam, M. K.; Niu, Y.; Hussain, T.; Tabassum, H.; Tang, W.; Xu, M.; Ahuja, R. (2021). How to avoid dendrite formation in metal batteries: innovative strategies for dendrite suppression. Nano Energy *86*, 106142.
20. Zhang, Y.; Wang, C.; Pastel, G.; Kuang, Y.; Xie, H.; Li, Y.; Liu, B.; Luo, W.; Chen, C.; Hu, L. (2018). 3D wettable framework for dendrite‐free alkali metal anodes. Advanced Energy Materials *8*, 1800635.
21. Jäckle, M.; Helmbrecht, K.; Smits, M.; Stottmeister, D.; Groß, A. (2018). Self-diffusion barriers: possible descriptors for dendrite growth in batteries? Energy & Environmental Science *11*, 3400-3407.

22. Vishnugopi, B. S.; Hao, F.; Verma, A.; Mukherjee, P. P. (2020). Surface diffusion manifestation in electrodeposition of metal anodes. Physical Chemistry Chemical Physics *22*, 11286-11295.
23. Chen, S.; Zheng, J.; Yu, L.; Ren, X.; Engelhard, M. H.; Niu, C.; Lee, H.; Xu, W.; Xiao, J.; Liu, J.; Zhang, J.-G. (2018). High-Efficiency Lithium Metal Batteries with Fire-Retardant Electrolytes. Joule *2*, 1548-1558.
24. Seh, Z. W.; Sun, J.; Sun, Y.; Cui, Y. (2015). A Highly Reversible Room-Temperature Sodium Metal Anode. ACS Central Science *1*, 449-455.
25. Schafzahl, L.; Hanzu, I.; Wilkening, M.; Freunberger, S. A. (2017). An Electrolyte for Reversible Cycling of Sodium Metal and Intercalation Compounds. ChemSusChem *10*, 401-408.
26. Aurbach, D.; Zaban, A. (1993). Impedance spectroscopy of lithium electrodes: Part 1. General behavior in propylene carbonate solutions and the correlation to surface chemistry and cycling efficiency. Journal of Electroanalytical Chemistry *348*, 155-179.
27. Cao, R.; Mishra, K.; Li, X.; Qian, J.; Engelhard, M. H.; Bowden, M. E.; Han, K. S.; Mueller, K. T.; Henderson, W. A.; Zhang, J.-G. (2016). Enabling room temperature sodium metal batteries. Nano Energy *30*, 825-830.
28. Bouibes, A.; Takenaka, N.; Fujie, T.; Kubota, K.; Komaba, S.; Nagaoka, M. (2018). Concentration Effect of Fluoroethylene Carbonate on the Formation of Solid Electrolyte Interphase Layer in Sodium-Ion Batteries. ACS Applied Materials & Interfaces *10*, 28525-28532.
29. Chen, R.; Qu, W.; Guo, X.; Li, L.; Wu, F. (2016). The pursuit of solid-state electrolytes for lithium batteries: from comprehensive insight to emerging horizons. Materials Horizons *3*, 487-516.
30. Song, S.; Kotobuki, M.; Zheng, F.; Xu, C.; Savilov, S. V.; Hu, N.; Lu, L.; Wang, Y.; Li, W. D. Z. (2017). A hybrid polymer/oxide/ionic-liquid solid electrolyte for Na-metal batteries. Journal of Materials Chemistry A *5*, 6424-6431.
31. Ansari, Y.; Guo, B.; Cho, J. H.; Park, K.; Song, J.; Ellison, C. J.; Goodenough, J. B. (2014). Low-Cost, Dendrite-Blocking Polymer-Sb2O3Separators for Lithium and Sodium Batteries. Journal of The Electrochemical Society *161*, A1655-A1661.
32. Wei, T.; Gong, Y.; Zhao, X.; Huang, K. (2014). An All-Ceramic Solid-State Rechargeable Na+-Battery Operated at Intermediate Temperatures. Advanced Functional Materials *24*, 5380-5384.
33. Wei, S.; Choudhury, S.; Xu, J.; Nath, P.; Tu, Z.; Archer, L. A. (2017). Highly Stable Sodium Batteries Enabled by Functional Ionic Polymer Membranes. Advanced Materials *29*, 1605512.
34. Choudhury, S.; Wei, S.; Ozhabes, Y.; Gunceler, D.; Zachman, M. J.; Tu, Z.; Shin, J. H.; Nath, P.; Agrawal, A.; Kourkoutis, L. F.; Arias, T. A.; Archer, L. A. (2017). Designing solid-liquid interphases for sodium batteries. Nat Commun *8*, 898.
35. Cheng, X.-B.; Zhang, R.; Zhao, C.-Z.; Zhang, Q. (2017). Toward Safe Lithium Metal Anode in Rechargeable Batteries: A Review. Chemical Reviews *117*, 10403-10473.
36. Luo, W.; Lin, C.-F.; Zhao, O.; Noked, M.; Zhang, Y.; Rubloff, G. W.; Hu, L. (2017). Ultrathin Surface Coating Enables the Stable Sodium Metal Anode. Advanced Energy Materials *7*, 1601526.
37. Fan, L.; Zhuang, H. L.; Gao, L.; Lu, Y.; Archer, L. A. (2017). Regulating Li deposition at artificial solid electrolyte interphases. Journal of Materials Chemistry A *5*, 3483-3492.

38. Zhao, Y.; Goncharova, L. V.; Lushington, A.; Sun, Q.; Yadegari, H.; Wang, B.; Xiao, W.; Li, R.; Sun, X. (2017). Superior Stable and Long Life Sodium Metal Anodes Achieved by Atomic Layer Deposition. Advanced Materials *29*, 1606663.
39. Tikekar, M. D.; Choudhury, S.; Tu, Z.; Archer, L. A. (2016). Design principles for electrolytes and interfaces for stable lithium-metal batteries. Nature Energy *1*, 16114.
40. Parimalam, B. S.; MacIntosh, A. D.; Kadam, R.; Lucht, B. L. (2017). Decomposition Reactions of Anode Solid Electrolyte Interphase (SEI) Components with LiPF6. The Journal of Physical Chemistry C *121*, 22733-22738.
41. Dey, A. N.; Sullivan, B. P. (1970). The Electrochemical Decomposition of Propylene Carbonate on Graphite. Journal of The Electrochemical Society *117*, 222.
42. Peled, E. (1979). The Electrochemical Behavior of Alkali and Alkaline Earth Metals in Nonaqueous Battery Systems—The Solid Electrolyte Interphase Model. Journal of The Electrochemical Society *126*, 2047-2051.
43. Lee, J.; Kim, J.; Kim, S.; Jo, C.; Lee, J. (2020). A review on recent approaches for designing the SEI layer on sodium metal anodes. Materials Advances *1*, 3143-3166.
44. Cohn, A. P.; Muralidharan, N.; Carter, R.; Share, K.; Pint, C. L. (2017). Anode-Free Sodium Battery through in Situ Plating of Sodium Metal. Nano Letters *17*, 1296-1301.
45. Iermakova, D. I.; Dugas, R.; Palacín, M. R.; Ponrouch, A. (2015). On the Comparative Stability of Li and Na Metal Anode Interfaces in Conventional Alkyl Carbonate Electrolytes. Journal of The Electrochemical Society *162*, A7060-A7066.
46. Kumar, H.; Detsi, E.; Abraham, D. P.; Shenoy, V. B. (2016). Fundamental Mechanisms of Solvent Decomposition Involved in Solid-Electrolyte Interphase Formation in Sodium Ion Batteries. Chemistry of Materials *28*, 8930-8941.
47. Thenuwara, A. C.; Shetty, P. P.; Kondekar, N.; Sandoval, S. E.; Cavallaro, K.; May, R.; Yang, C.-T.; Marbella, L. E.; Qi, Y.; Mcdowell, M. T. (2020). Efficient Low-Temperature Cycling of Lithium Metal Anodes by Tailoring the Solid-Electrolyte Interphase. ACS Energy Letters *5*, 2411-2420.
48. Pei, A.; Zheng, G.; Shi, F.; Li, Y.; Cui, Y. (2017). Nanoscale Nucleation and Growth of Electrodeposited Lithium Metal. Nano Letters *17*, 1132-1139.
49. Biswal, P.; Stalin, S.; Kludze, A.; Choudhury, S.; Archer, L. A. (2019). Nucleation and Early Stage Growth of Li Electrodeposits. Nano Letters *19*, 8191-8200.
50. Macdonald, D. D. (1992). The Point Defect Model for the Passive State. Journal of The Electrochemical Society *139*, 3434-3449.
51. Chao, C. Y.; Lin, L. F.; Macdonald, D. D. (1981). A Point Defect Model for Anodic Passive Films: I . Film Growth Kinetics. Journal of The Electrochemical Society *128*, 1187-1194.
52. Shi, F.; Pei, A.; Boyle, D. T.; Xie, J.; Yu, X.; Zhang, X.; Cui, Y. (2018). Lithium metal stripping beneath the solid electrolyte interphase. Proceedings of the National Academy of Sciences *115*, 8529-8534.
53. Kim, H.; Gong, Y. J.; Yoo, J.; Kim, Y. S. (2018). Highly stable lithium metal battery with an applied three-dimensional mesh structure interlayer. Journal of Materials Chemistry A *6*, 15540-15545.
54. Carter, R.; NewRingeisen, A.; Reed, D.; Atkinson, R. W.; Mukherjee, P. P.; Love, C. T. (2021). Optical Microscopy Reveals the Ambient Sodium–Sulfur Discharge Mechanism. ACS Sustainable Chemistry & Engineering *9*, 92-100.
55. Mistry, A.; Fear, C.; Carter, R.; Love, C. T.; Mukherjee, P. P. (2019). Electrolyte Confinement Alters Lithium Electrodeposition. ACS Energy Letters *4*, 156-162.

56. Frenck, L.; Sethi, G. K.; Maslyn, J. A.; Balsara, N. P. (2019). Factors That Control the Formation of Dendrites and Other Morphologies on Lithium Metal Anodes. Frontiers in Energy Research *7*.
57. Boyle, D. T.; Kim, S. C.; Oyakhire, S. T.; Vilá, R. A.; Huang, Z.; Sayavong, P.; Qin, J.; Bao, Z.; Cui, Y. (2022). Correlating Kinetics to Cyclability Reveals Thermodynamic Origin of Lithium Anode Morphology in Liquid Electrolytes. Journal of the American Chemical Society *144*, 20717-20725.
58. Nanbu, N.; Suzuki, K.; Yagi, N.; Sugahara, M.; Takehara, M.; Ue, M.; Sasaki, Y. (2007). Use of Fluoroethylene Carbonate as Solvent for Electric Double-Layer Capacitors. Electrochemistry *75*, 607-610.
59. Tobishima, S.-I.; Okada, T. (1985). Lithium cycling efficiency and conductivity for high dielectric solvent/low viscosity solvent mixed systems. Electrochimica Acta *30*, 1715-1722.
60. Voter, A. F., Introduction to the Kinetic Monte carlo Method. Springer Netherlands: pp 1-23.
61. Vishnugopi, B. S.; Hao, F.; Verma, A.; Mukherjee, P. P. (2020). Double-Edged Effect of Temperature on Lithium Dendrites. ACS Applied Materials & Interfaces *12*, 23931-23938.
62. Vishnugopi, B. S.; Dixit, M. B.; Hao, F.; Shyam, B.; Cook, J. B.; Hatzell, K. B.; Mukherjee, P. P. (2021). Mesoscale Interrogation Reveals Mechanistic Origins of Lithium Filaments along Grain Boundaries in Inorganic Solid Electrolytes. Advanced Energy Materials *12*.
63. Jäckle, M.; Helmbrecht, K.; Smits, M.; Stottmeister, D.; Groß, A. (2018). Self-diffusion barriers: possible descriptors for dendrite growth in batteries? Energy & Environmental Science *11*, 3400-3407.
64. Bouibes, A.; Takenaka, N.; Kubota, K.; Komaba, S.; Nagaoka, M. (2022). Development of advanced electrolytes in Na-ion batteries: application of the Red Moon method for molecular structure design of the SEI layer. RSC Advances *12*, 971-984.
65. Li, K.; Zhang, J.; Lin, D.; Wang, D.-W.; Li, B.; Lv, W.; Sun, S.; He, Y.-B.; Kang, F.; Yang, Q.-H.; Zhou, L.; Zhang, T.-Y. (2019). Evolution of the electrochemical interface in sodium ion batteries with ether electrolytes. Nat Commun *10*.
66. Bock, D. C.; Waller, G. H.; Mansour, A. N.; Marschilok, A. C.; Takeuchi, K. J.; Takeuchi, E. S. (2018). Investigation of Solid Electrolyte Interphase Layer Formation and Electrochemical Reversibility of Magnetite, Fe3O4, Electrodes: A Combined X-ray Absorption Spectroscopy and X-ray Photoelectron Spectroscopy Study. The Journal of Physical Chemistry C *122*, 14257-14271.
67. Eshetu, G. G.; Grugeon, S.; Kim, H.; Jeong, S.; Wu, L.; Gachot, G.; Laruelle, S.; Armand, M.; Passerini, S. (2016). Comprehensive Insights into the Reactivity of Electrolytes Based on Sodium Ions. ChemSusChem *9*, 462-471.
68. Fondard, J.; Irisarri, E.; Courrèges, C.; Palacin, M. R.; Ponrouch, A.; Dedryvère, R. (2020). SEI Composition on Hard Carbon in Na-Ion Batteries After Long Cycling: Influence of Salts (NaPF6, NaTFSI) and Additives (FEC, DMCF). Journal of The Electrochemical Society *167*, 070526.
69. Love, C. T.; Baturina, O. A.; Swider-Lyons, K. E. (2014). Observation of Lithium Dendrites at Ambient Temperature and Below. ECS Electrochemistry Letters *4*, A24-A27.

Supporting Information

Fluorinated Ethylene Carbonate as Additive to Glyme Electrolytes for Robust Sodium Solid Electrolyte Interface

Susmita Sarkar[1+], Matthew J. Lefler[2+], Bairav S. Vishnugopi[1], R. Blake Nuwayhid[2], Corey T. Love[2], Rachel Carter[2]*, and Partha P. Mukherjee[1]*

[1] School of Mechanical Engineering, Purdue University, West Lafayette, Indiana 47907, USA

[2] NRC/NRL, U. S. Naval Research Laboratory, Washington, DC 20375, USA

[3] Chemistry Division, U. S. Naval Research Laboratory, Washington, DC 20375, USA

Table S1: Nucleation overpotential ($\boldsymbol{\eta_{nu}}$), plateau overpotential ($\boldsymbol{\eta_{pl}}$), and the impedance of sodium deposited on copper in glyme solvents

Solvent	$\boldsymbol{\eta_{nu}}$ **(mV)**	$\boldsymbol{\eta_{pl}}$ **(mV)**	$\mathbf{R_{SEI}+R_{CT}}$ **(Ω)**
G_1	29.8	2.4	50.6
G_2	13.6	3.1	28.9
G_4	19.9	5.8	42.5

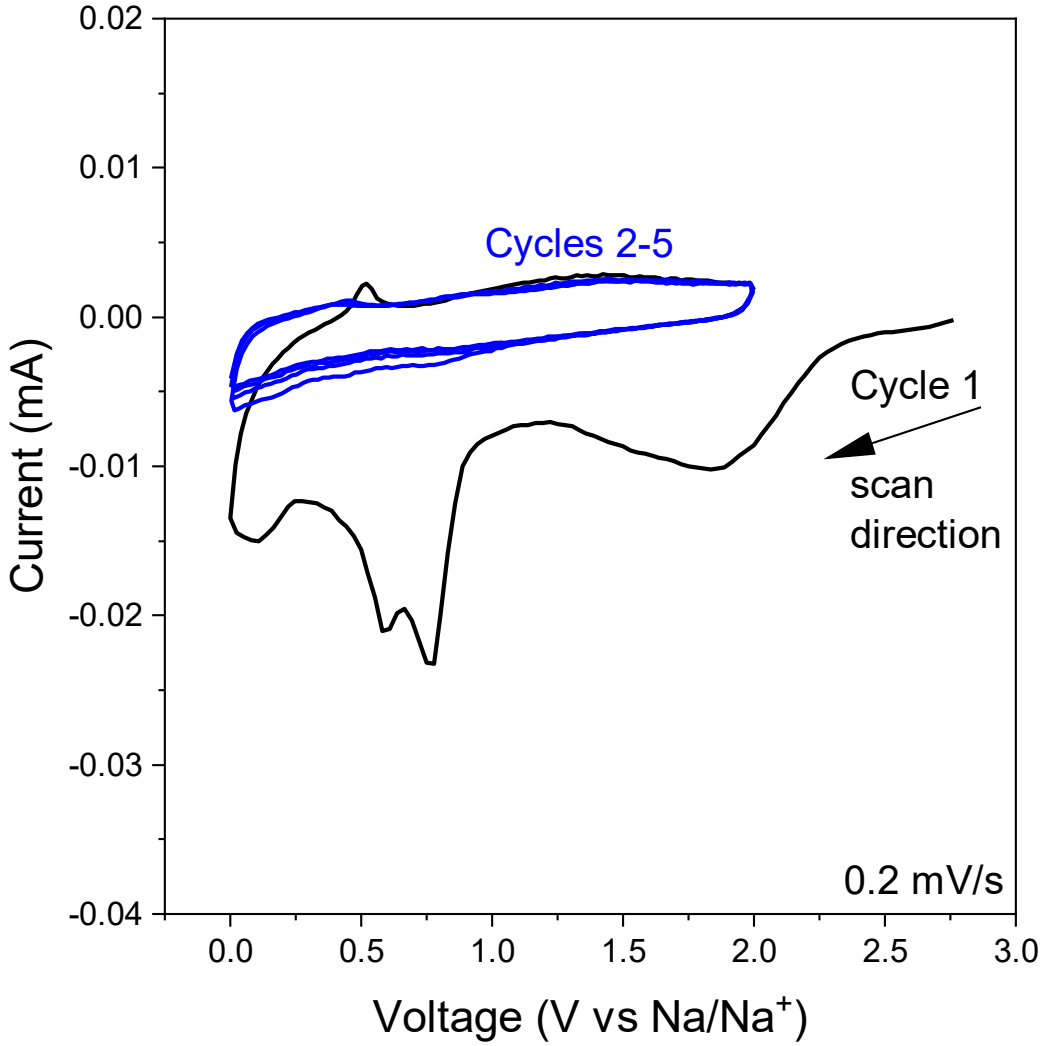

Figure S1. Cyclic voltammetry of Na|Cu in 1M $NaPF_6$ showing irreversible reductive peaks in cycle 1 only.

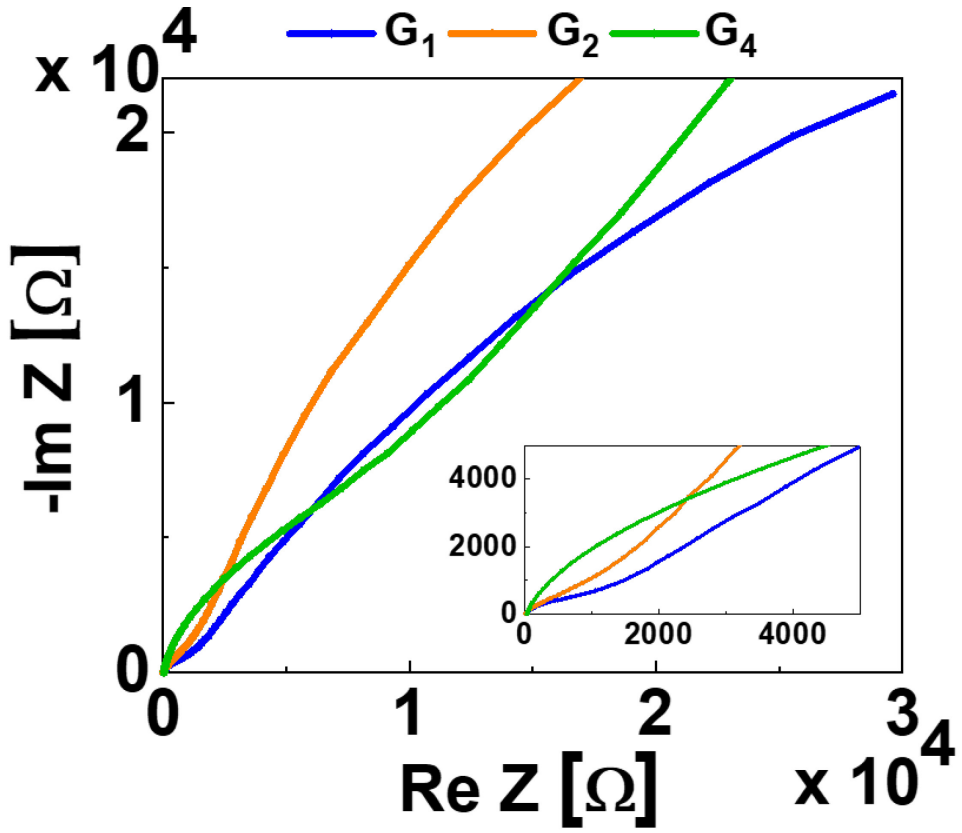

Figure S2. EIS of Fresh Na-Cu cells in $NaPF_6$: G_1, $NaPF_6$: G_2 and $NaPF_6$: G_4.

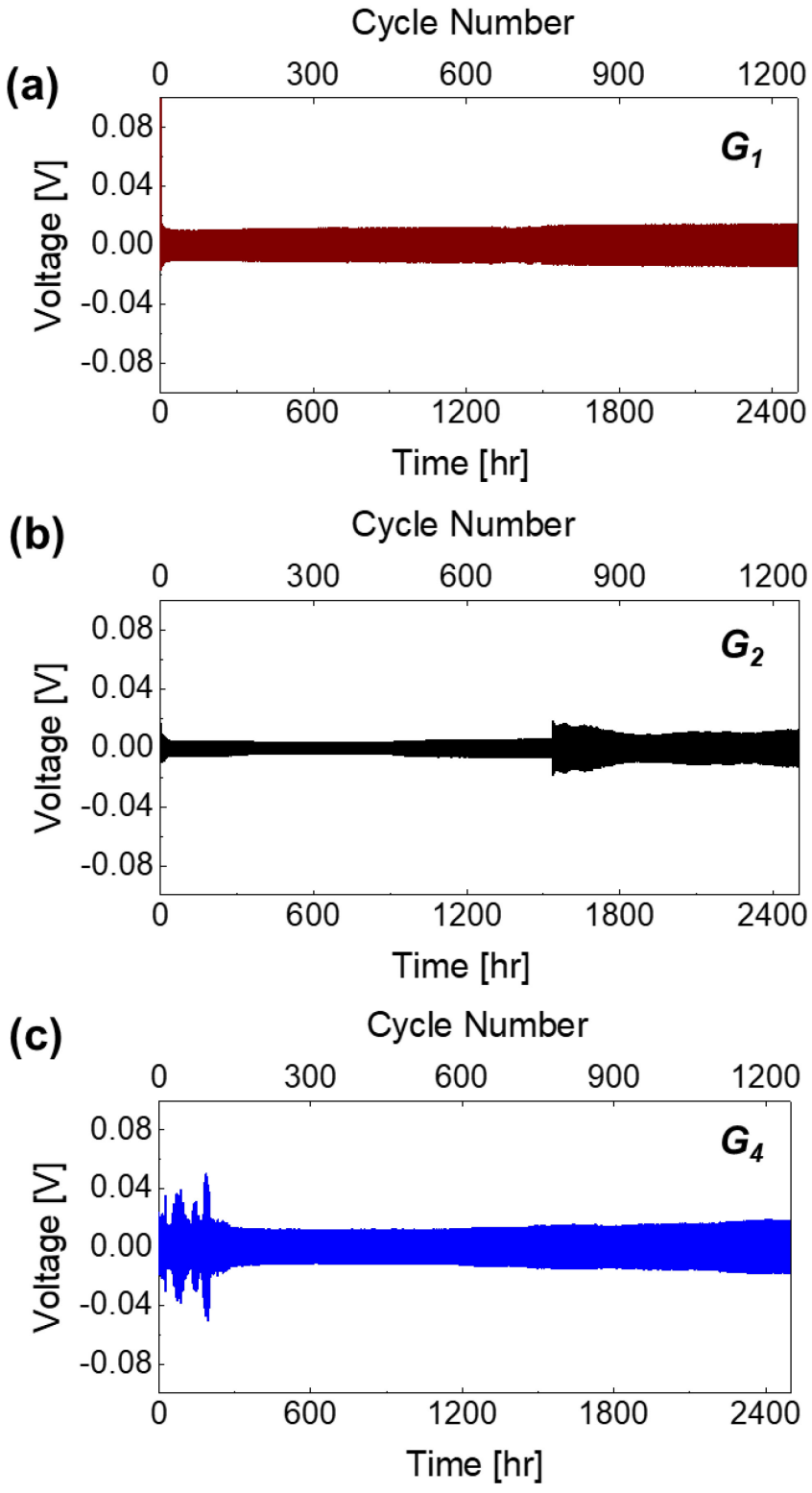

Figure S3. Plating-stripping profile of Na-Na cells in different electrolyte at 0.5 mA/cm^2 and 0.5 mAh/cm^2 (a) G_1 (b) G_2 and (c) G_4.

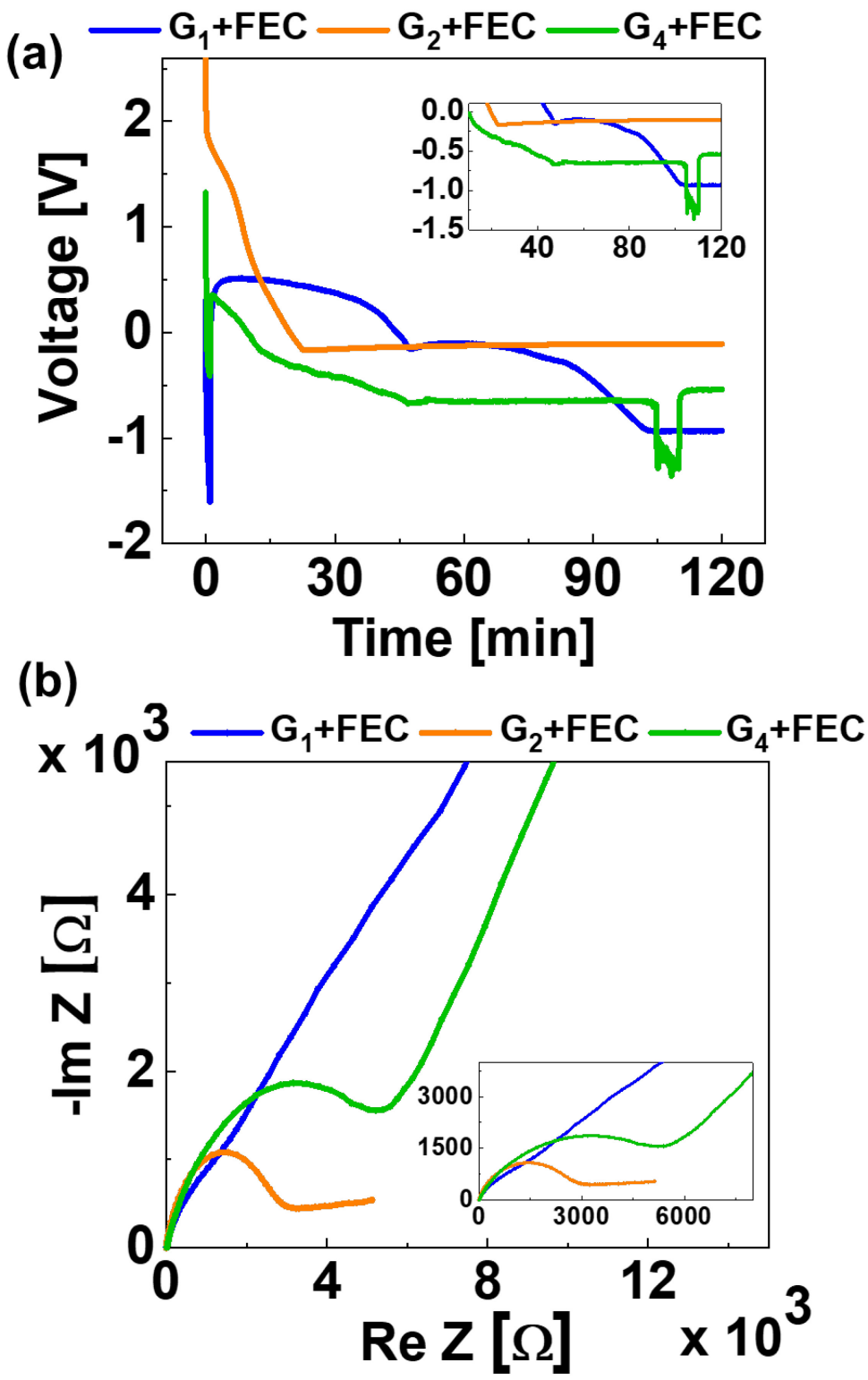

Figure S4. (a) Discharge curve of Na-Cu cells in different electrolyte at 0.02 mA/cm^2 and 0.04 mAh/cm^2. (b) EIS of the Na-Cu cells after 1 discharge in different electrolytes. The electrolytes are $NaPF_6$: G_1+FEC, $NaPF_6$: G_2+FEC and $NaPF_6$: G_4+FEC.

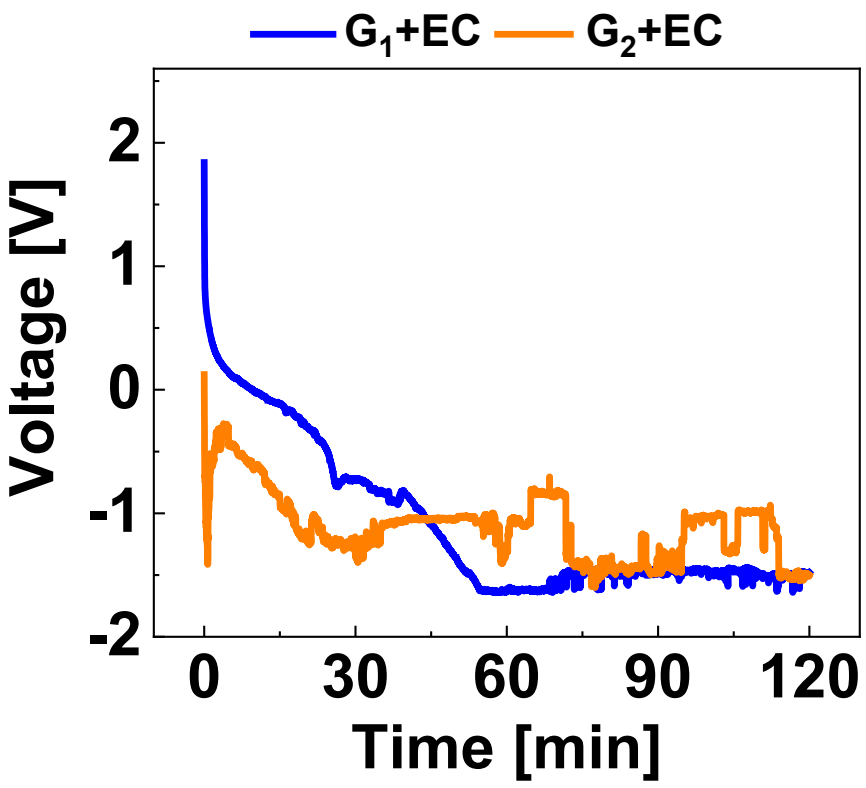

Figure S5. Discharge curve of Na-Cu cells in different electrolyte at 0.02mA/cm^2 and 0.04 mAh/cm^2. The electrolytes are $NaPF_6$: G_1+EC and $NaPF_6$: G_2+EC.

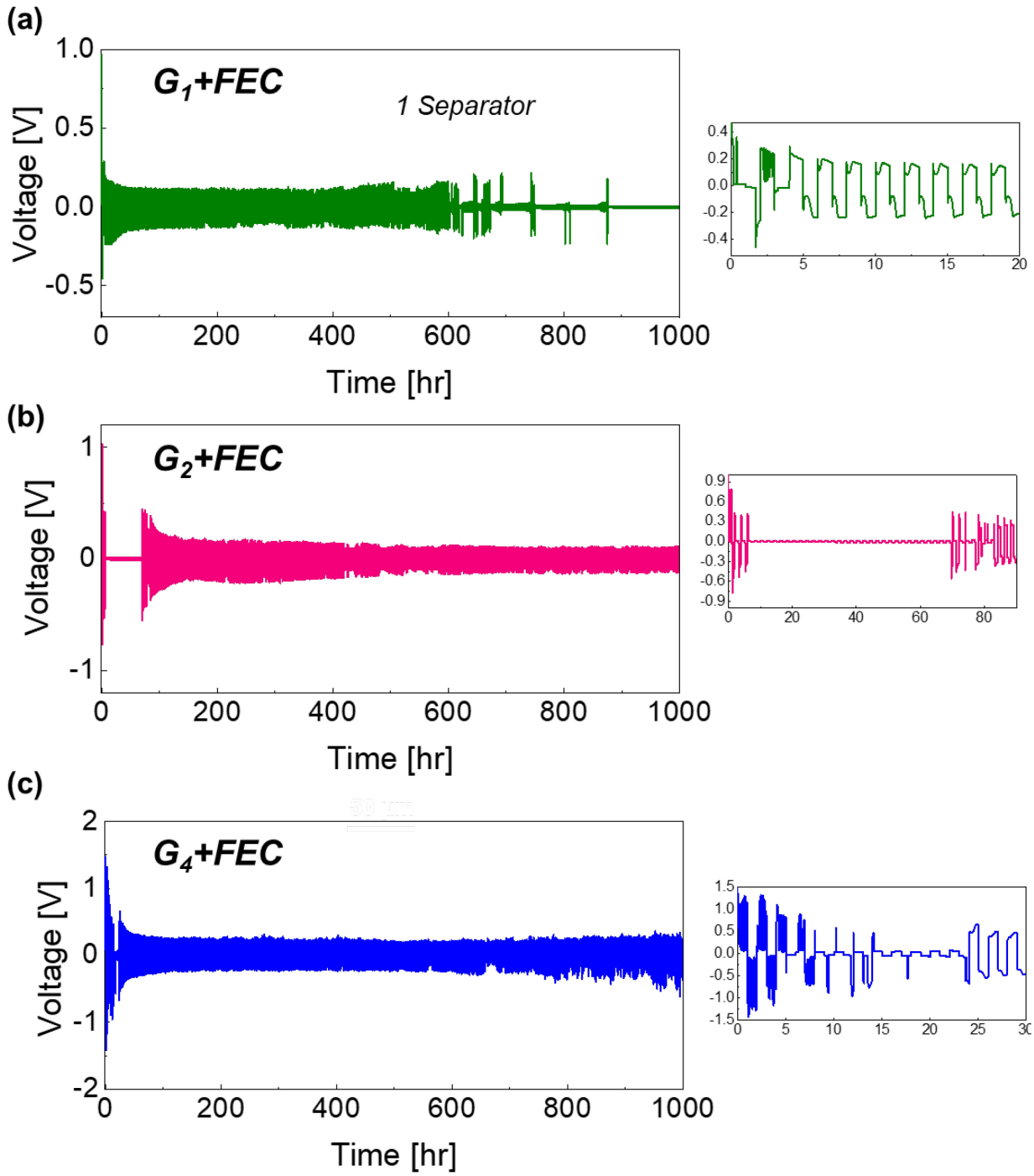

Figure S6. Charge-Discharge curve of Na-Na cells in different electrolyte at 0.05 mA/cm^2 and 0.1 mAh/cm^2 using 1 Enetek Separator. The electrolytes are $NaPF_6$: G_1+FEC and $NaPF_6$: G_2+FEC and $NaPF_6$: G_4+FEC.

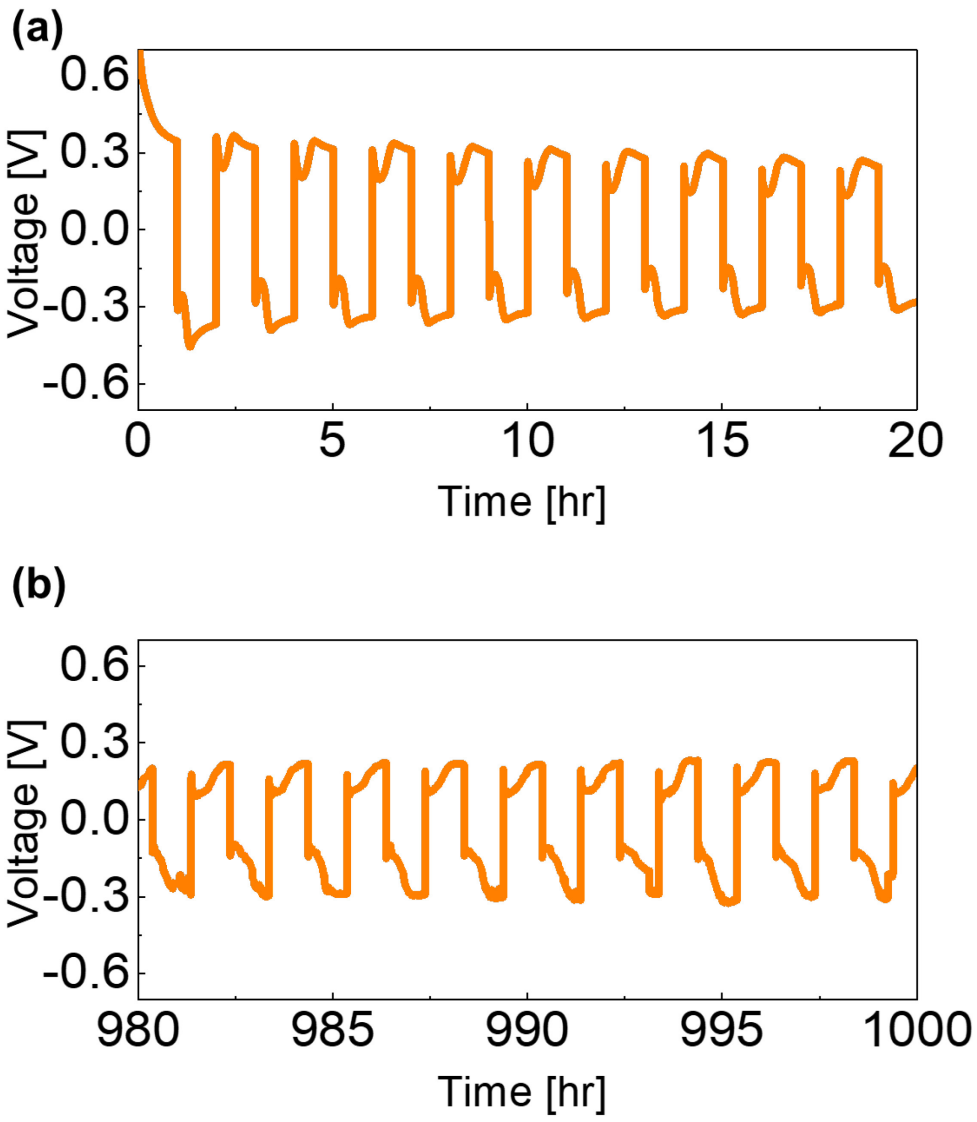

Figure S7. Zoomed in of charge-discharge curve (a) Early and (b) Later cycle of Na-Na cells in $NaPF_6$: G_2+FEC electrolyte at 0.5 mA/cm^2 and 0.5 mAh/cm^2 using 2 Enetek Separator.

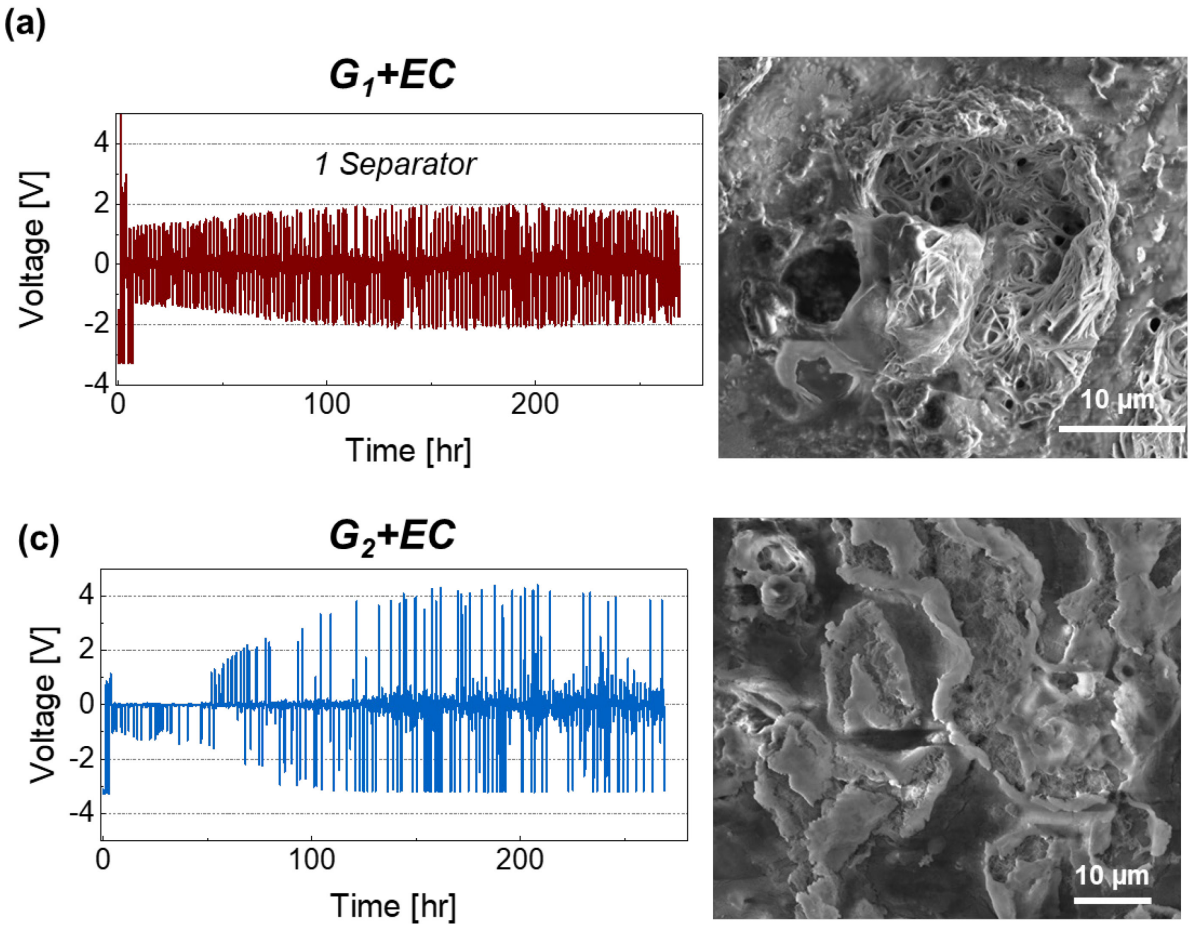

Figure S8. Charge-Discharge curve of Na-Na cells in different electrolyte at 0.05 mA/cm^2 and 0.1 mAh/cm^2 using 1 Enetek Separator. The electrolytes are $NaPF_6$: G_1+EC and $NaPF_6$: G_2+EC.

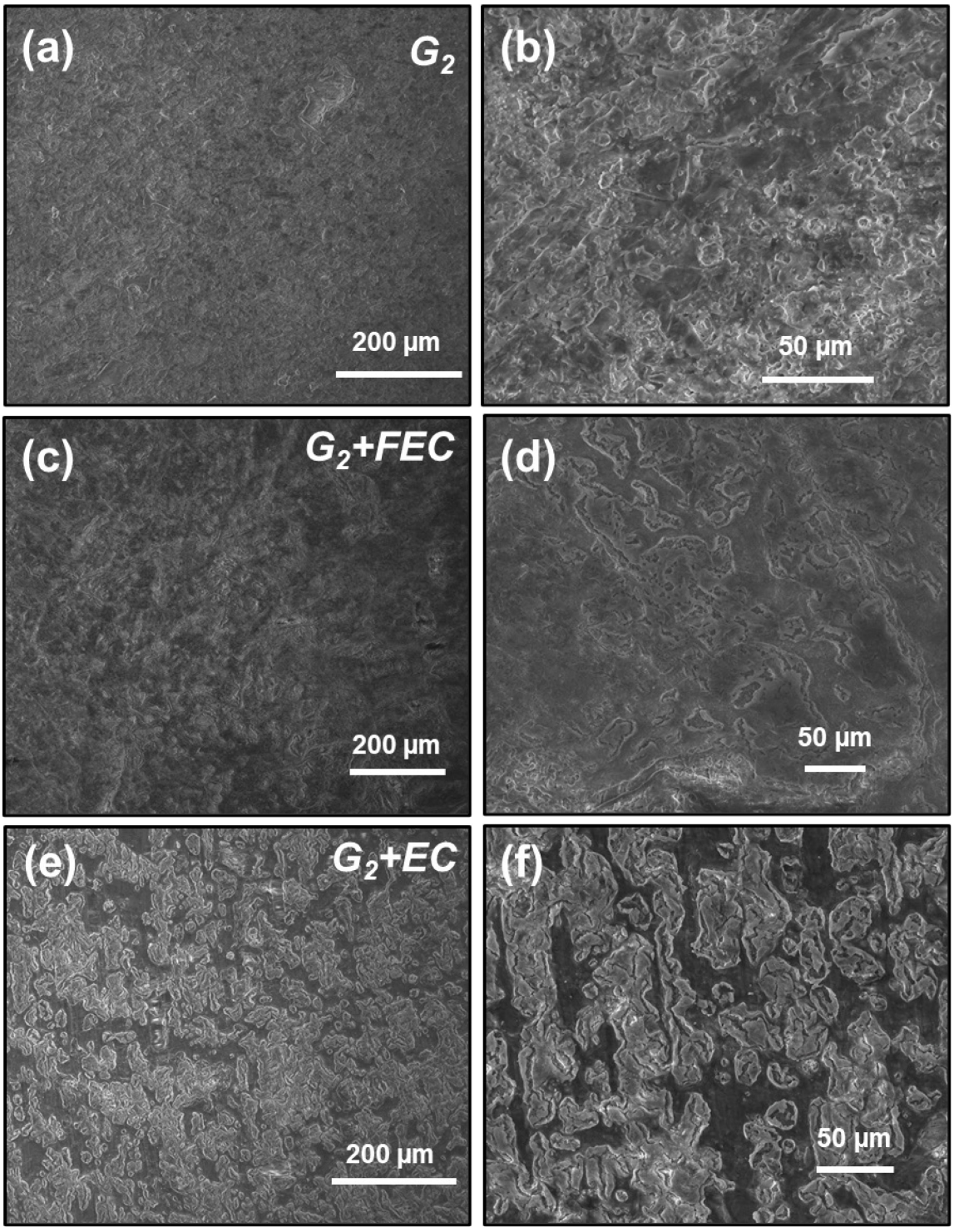

Figure S9. SEM Images of the Na foil after 10 charge-discharge cycles (a)-(b) G_2, (c)-(d) G_2+FEC and (e)-(f) G_2+EC

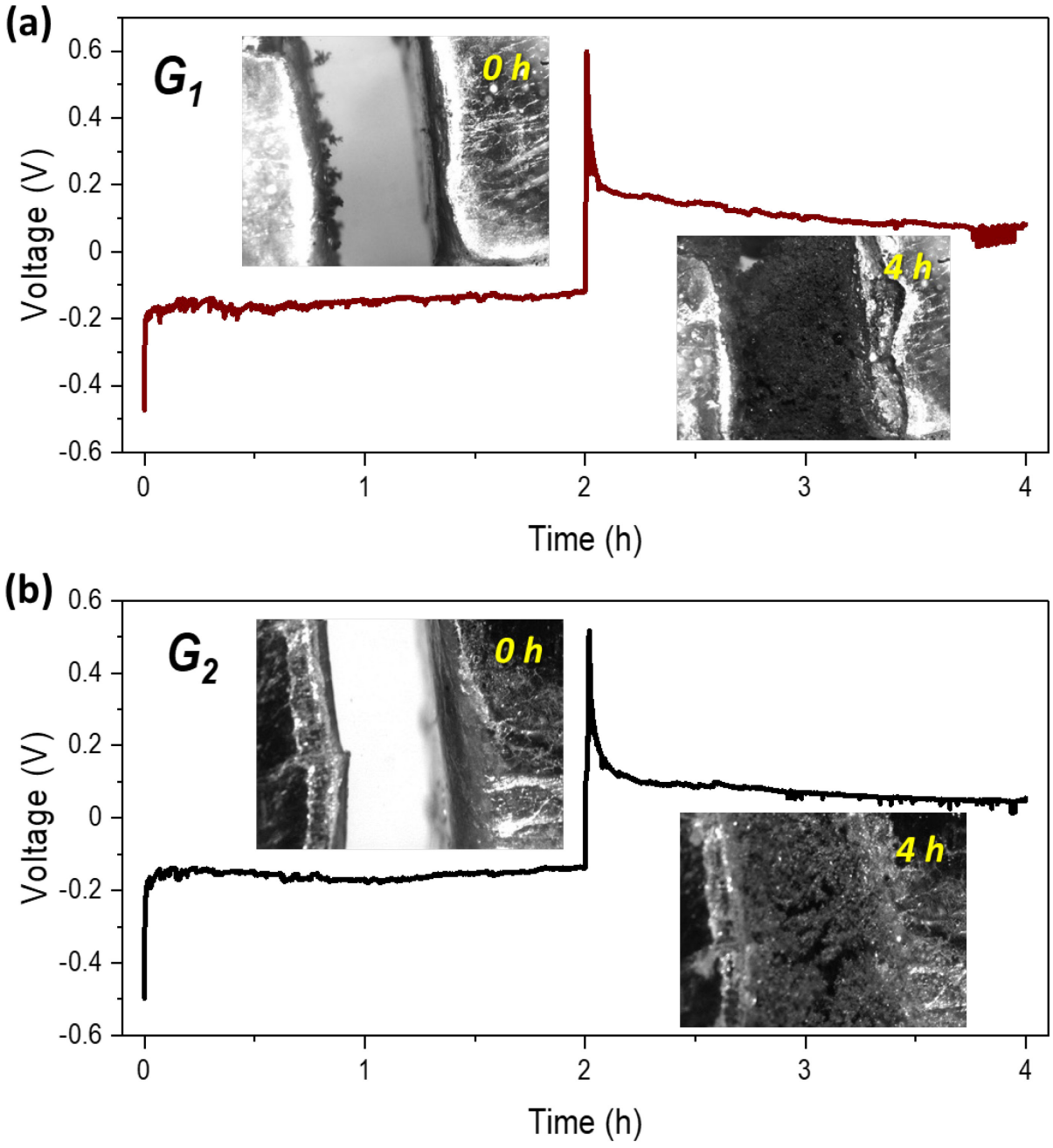

Figure S10. Voltage profiles and optical cell images of Na|Na symmetric cells with (a) G_1 and (b) G_2 electrolyte.

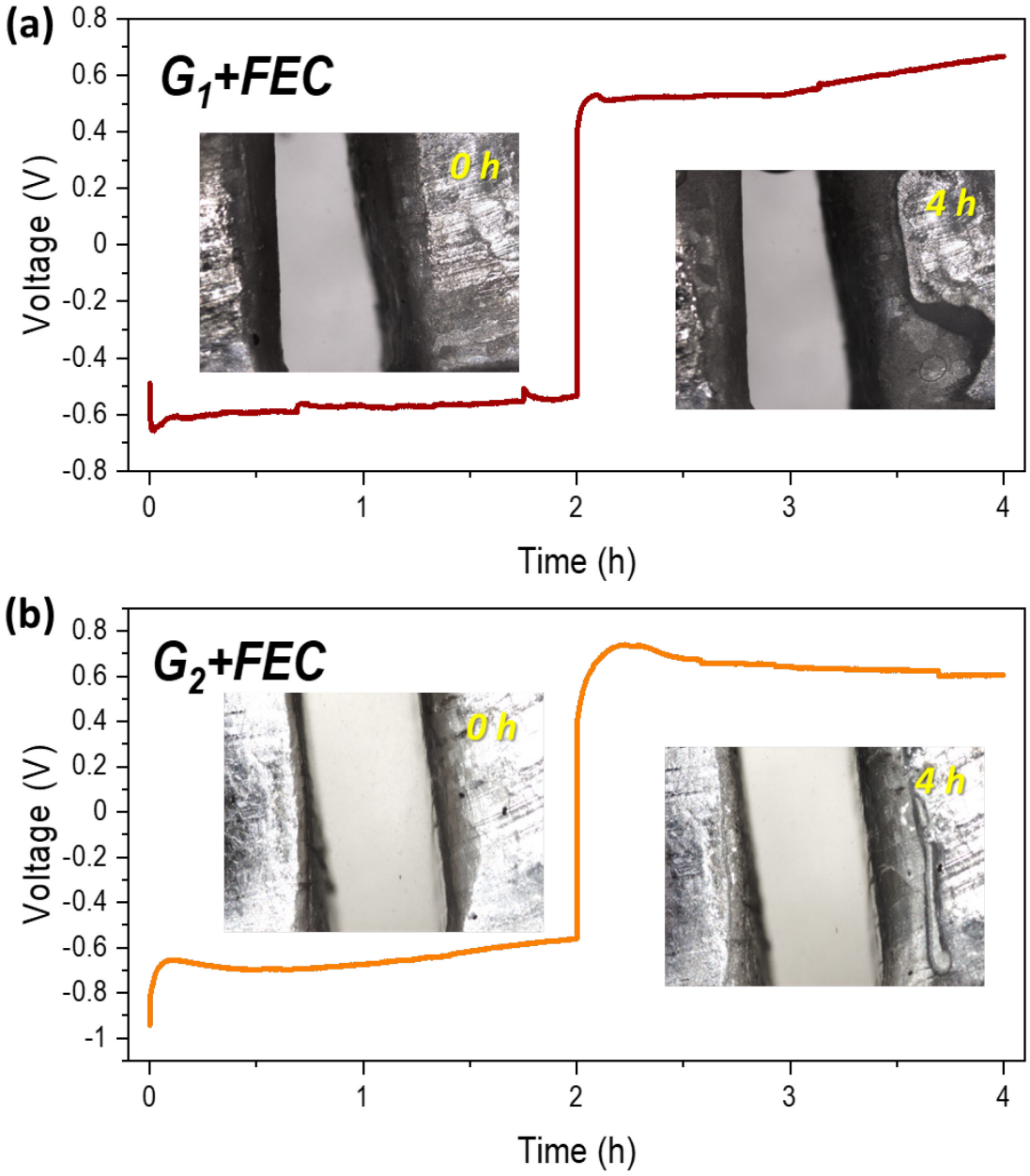

Figure S11. Voltage profiles and optical cell images of Na|Na symmetric cells with (a) G_1 and (b) G_2 electrolyte with 10% by volume (~1.4M) FEC additive.

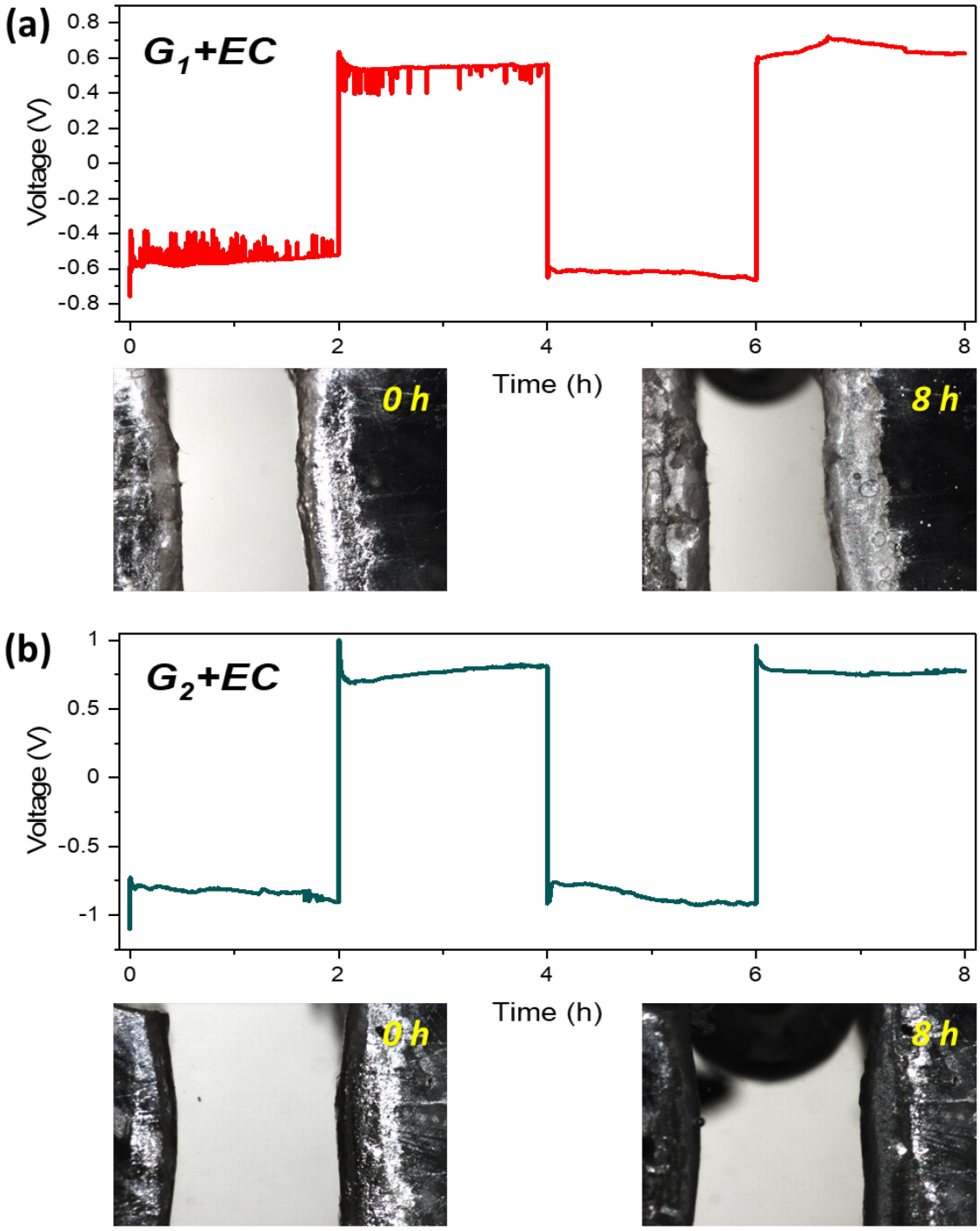

Figure S12. Voltage profiles and optical cell images of Na|Na symmetric cells with (a) G_1 and (b) G_2 electrolyte with 1.4M EC additive.

Table S2: XPS Peak Assignments for Electrodes Cycled 10× G2, G2-FEC and g2-EC-Containing Electrolytes

Elements	G2	G2+FEC	G2+EC	Chemistry
C 1s	285	284.8	284.78	C-C, C-H
	286.5	286.12	286.44	C-O
	288.54	288.5	288.87	O-C=O
O 1s	530.16	529.96		Na-O
	531.64	531.50	531.19	C=O
	533.13	533.10	533.02	C-O / FEC
	536.10	536.26	536.21	Na auger
F 1s	684.31	684.17	684.02	NaF
	687.42	687.04	687.19	P-F
	689.89	689.55		C-F
Na 1s	1071.89	1071.37	1071.71	NaF, RONa, Na_2CO_3
P 2p	134.06	133.55	133.79	P_2O_5, $Na_xPO_yF_z$
			137.24	Na_xPF_y

Table S3. Survey of the performances of "state-of-the-art" craboante-ether electrolyte mixtures in Li and N metal batteries.

Salts	*Solvents*	*Year / Refs.*
$LiPF_6$ / $LiAsF_6$ / LiTFSI	EC-PC-DME	(1994) [1]
$LiClO_4$	EC-DME / PC-DME /	(1984)

	EC-PC-DME	[2]
LiBF4 / LiCF3SO3 / LiClO4 / LiAsF6	EC/PC-THF/DME/DOL/DEE	*(1985)* [3]
	DME-EC	*2017* [4]
LiNO3	DME-FEC	*2018* [5]
LiFSI	DME-FEC	*2020* [6]
	DOL-DME-FEC	*2020* [7]
	DME-FEC	*2021* [8]
NaClO4	DME/DOL (v:v = 1:1) + 5 wt% FEC	*2019* [9]
NaPF6	Diglyme+FEC	*2020* [10]
LiPF6	TEGDME-FEC	*2013* [11]
LiTFSI	TEGDME-FEC	*2015* [12]
LiF3SO3	TEGDME-FEC (5:1 v/v)	*2015* [13]
LiTFSI	TEGDME-FEC	*2018* [14]
NaTFSI	TEGDME-FEC	*2019* [15]

Description of the mesoscale modeling framework

The mesoscale model captures the morphological growth of the metal electrode based on the kinetic Monte Carlo algorithm.[16-18] The evolution of the metal electrode interface including the processes of ion transport, electrochemical reaction and self-diffusion have been incorporated in the model.

For each of these processes, a corresponding kinetic rate is calculated as described below. The substrate-Na interaction and the early stage morphological growth is studied using the descriptor,

$k_{\text{Na-substrate}}/k_{\text{Na-Na}}$. Here, $k_{\text{Na-substrate}}$ denotes the rate of Na reduction on the substrate and $k_{\text{Na-Na}}$ denotes the rate of Na reduction on the freshly deposited Na. These two processes are used to define a total reaction rate (k_1) as follows:

$$k_1 = \sum_{i=1}^{N_1} k^i_{Na-substrate} + \sum_{j=1}^{N_1^|} k^j_{Na-Na} \tag{S1}$$

Here, N_1 is the number of metal ions at the substrate-electrolyte interface and $N_1^|$ is the number of metal ions at the freshly deposited metal and electrolyte interface.

For the self-diffusion of the deposited metal atoms,

$$k_2 = \sum_{i=1}^{N_2} k^i_D \tag{S2}$$

Here, N_2 is the number of deposited atoms, and k_D is the surface self-diffusion rate of the deposited atoms that is calculated based on the Arrhenius equation, $k_D = \nu\, exp\left(\frac{-E_{a,d}}{k_b T}\right)$. Here, ν is the hopping frequency, k_b is the Boltzmann constant, T is the temperature, $E_{a,d}$ is the energy barrier, and k_2 refers to the total self-diffusion rate.

For ionic transport, a total rate, k_3 is calculated as follows:

$$k_3 = \sum_{i=1}^{N_3} k^i_T \tag{S3}$$

Here, N_3 is the number of metal ions in the system, and k_T refers to the transport rate of each ion, which is calculated using $k_T = \frac{D}{d^2}$. D refers to the diffusivity for ion transport, and d is the distance per diffusion step, given by $d = \sqrt{2}a$. Here, a is the lattice size.

Based on k_1, k_2 and k_3, a total rate constant (k_{total}) is defined as follows:

$$k_{total} = \sum_{i=1}^{3} k_i \tag{S4}$$

A random number r_1, between 0 to 1 is chosen and multiplied with k_{total}. Subsequently, all the possible processes for evolving the system are scanned through, and the first event for which the total rate of previously scanned events is larger than $r_1 k_{total}$ is chosen. The electrochemical system is then evolved using this selected event. The time step associated with this process is

calculated using a random number, r_2: $\delta t = -\frac{1}{k_{total}} \ln r_2$. The parameters used in the mesoscale model to capture the metal morphology evolution have been summarized below in Table S4.

Table S4. Parameters used in the model.

Parameters		**Values**	**Units**
	System dimensions	100 × 60 lattice supercell	-
a	Lattice size (for Na)	4.29	Å
D	Diffusivity (ion transport)	3×10^{-10}	m^2/s
$E_{a,d}$	Surface self-diffusion barrier	0.1-0.4	eV
$k_{Na-substrate}$ / k_{Na-Na}	Ratio of Na reduction rate on the substrate and Na reduction rate on freshly deposited Na	$10^{-4} – 10^{0}$	-
F	Faraday constant	96,487	$C\ mol^{-1}$
k_b	Boltzmann constant	1.38×10^{-23}	$J\ K^{-1}$
T	Temperature	300	K
ν	Hopping frequency	2×10^{12}	s^{-1}

References:

1. Fringant, C., Tranchant, A., and Messina, R. (1995). Behavior of lithium-electrolyte interface during cycling in some ether-carbonate and carbonate mixtures. Electrochimica Acta *40*, 513-523. 10.1016/0013-4686(94)00199-b.
2. Tobishima, S.-I., Yamaki, J.-I., and Okada, T. (1984). Ethylene carbonate/ether mixed solvents electrolyte for lithium batteries. Electrochimica Acta *29*, 1471-1476. 10.1016/0013-4686(84)87030-9.
3. Tobishima, S.-I., and Okada, T. (1985). Lithium cycling efficiency and conductivity for high dielectric solvent/low viscosity solvent mixed systems. Electrochimica Acta *30*, 1715-1722. 10.1016/0013-4686(85)87019-5.
4. Cresce, A.V., Russell, S.M., Borodin, O., Allen, J.A., Schroeder, M.A., Dai, M., Peng, J., Gobet, M.P., Greenbaum, S.G., Rogers, R.E., and Xu, K. (2017). Solvation behavior of carbonate-based electrolytes in sodium ion batteries. Physical Chemistry Chemical Physics *19*, 574-586. 10.1039/c6cp07215a.
5. Zhang, X.-Q., Chen, X., Cheng, X.-B., Li, B.-Q., Shen, X., Yan, C., Huang, J.-Q., and Zhang, Q. (2018). Highly Stable Lithium Metal Batteries Enabled by Regulating the Solvation of Lithium Ions in Nonaqueous Electrolytes. Angewandte Chemie *130*, 5399-5403. 10.1002/ange.201801513.
6. Han, X., and Sun, J. (2020). Design of a LiF-rich solid electrolyte interface layer through salt-additive chemistry for boosting fast-charging phosphorus-based lithium ion battery performance. Chemical Communications *56*, 6047-6049. 10.1039/d0cc01853h.
7. Thenuwara, A.C., Shetty, P.P., Kondekar, N., Sandoval, S.E., Cavallaro, K., May, R., Yang, C.-T., Marbella, L.E., Qi, Y., and Mcdowell, M.T. (2020). Efficient Low-Temperature Cycling of Lithium Metal Anodes by Tailoring the Solid-Electrolyte Interphase. ACS Energy Letters *5*, 2411-2420. 10.1021/acsenergylett.0c01209.
8. Zheng, X., Huang, L., Luo, W., Wang, H., Dai, Y., Liu, X., Wang, Z., Zheng, H., and Huang, Y. (2021). Tailoring Electrolyte Solvation Chemistry toward an Inorganic-Rich Solid-Electrolyte Interphase at a Li Metal Anode. ACS Energy Letters *6*, 2054-2063. 10.1021/acsenergylett.1c00647.
9. Li, S., Zeng, Z., Yang, J., Han, Z., Hu, W., Wang, L., Ma, J., Shan, B., and Xie, J. (2019). High Performance Room Temperature Sodium–Sulfur Battery by Eutectic Acceleration in Tellurium-Doped Sulfurized Polyacrylonitrile. ACS Applied Energy Materials *2*, 2956-2964. 10.1021/acsaem.9b00343.
10. Ghosh, S., Qi, Z., Wang, H., Martha, S.K., and Pol, V.G. (2020). Ultrafast, dry microwave superheating for the synthesis of an SbOx–GNP hybrid anode to investigate the Na-ion storage compatibility in ester and ether electrolytes. Chemical Communications *56*, 9663-9666. 10.1039/d0cc02858d.
11. Song, J.-H., Yeon, J.-T., Jang, J.-Y., Han, J.-G., Lee, S.-M., and Choi, N.-S. (2013). Effect of Fluoroethylene Carbonate on Electrochemical Performances of Lithium Electrodes and Lithium-Sulfur Batteries. Journal of The Electrochemical Society *160*, A873-A881. 10.1149/2.101306jes.
12. Heine, J., Hilbig, P., Qi, X., Niehoff, P., Winter, M., and Bieker, P. (2015). Fluoroethylene Carbonate as Electrolyte Additive in Tetraethylene Glycol Dimethyl Ether Based Electrolytes for Application in Lithium Ion and Lithium Metal Batteries. Journal of The Electrochemical Society *162*, A1094-A1101. 10.1149/2.0011507jes.
13. Liu, Q.C., Xu, J.J., Yuan, S., Chang, Z.W., Xu, D., Yin, Y.B., Li, L., Zhong, H.X., Jiang, Y.S., Yan, J.M., and Zhang, X.B. (2015). Artificial Protection Film on Lithium Metal

Anode toward Long-Cycle-Life Lithium-Oxygen Batteries. Adv Mater *27*, 5241-5247. 10.1002/adma.201501490.

14. Zhang, T., Yang, J., Zhu, J., Zhou, J., Xu, Z., Wang, J., Qiu, F., and He, P. (2018). A lithium-ion oxygen battery with a Si anode lithiated in situ by a Li3N-containing cathode. Chemical Communications *54*, 1069-1072. 10.1039/c7cc09024b.
15. Wang, L., Chen, X., Li, S., Yang, J., Sun, Y., Peng, L., Shan, B., and Xie, J. (2019). Effect of eutectic accelerator in selenium-doped sulfurized polyacrylonitrile for high performance room temperature sodium–sulfur batteries. Journal of Materials Chemistry A *7*, 12732-12739. 10.1039/c9ta02831e.
16. Voter, A.F. (2007). Introduction to the kinetic Monte Carlo method. In Radiation effects in solids, (Springer), pp. 1-23.
17. Hao, F., Verma, A., and Mukherjee, P.P. (2019). Electrodeposition stability of metal electrodes. Energy Storage Materials *20*, 1-6.
18. Vishnugopi, B.S., Hao, F., Verma, A., and Mukherjee, P.P. (2020). Surface diffusion manifestation in electrodeposition of metal anodes. Physical Chemistry Chemical Physics *22*, 11286-11295.